Topological Identification of Vortical Flow Structures in the Left Ventricle of the Heart

AUTHOR(S):

Sakajo, Takashi; Itatani, Keiichi

CITATION:

Sakajo, Takashi ...[et al]. Topological Identification of Vortical Flow Structures in the Left Ventricle of the Heart. SIAM Journal on Imaging Sciences 2023, 16(3): 1491-1519

ISSUE DATE:

2023-09

URL:

http://hdl.handle.net/2433/284722

SIAM J. IMAGING SCIENCES
Vol. 16, No. 3, pp. 1491–1519

Topological Identification of Vortical Flow Structures in the Left Ventricle of the Heart*

Takashi Sakajo† and Keiichi Itatani‡

Abstract. Vortical blood flow structures inside the heart's left ventricle (LV) play a crucial role in an efficient blood supply from the heart to organs. Recent medical imaging and computational technology progress have brought us blood flow visualization tools in echocardiography and cardiac MRI. However, there are still few tools to precisely capture the vortical flow structures since the flow is highly unsteady and turbulent. Because of the importance of vortex flow power force on the prognosis of cardiac functions in heart diseases, identifying the vortex flow structure without ambiguity is essential in medical science. In this paper, we propose a mathematical method to describe the topological features of two-dimensional (2D) flows with symbolic graph expressions, called COT representations. Since the heart contracts and relaxes repeatedly in a short time range, the instantaneous blood flow pattern along this moving boundary would appear as a source/sink structure. This means that the flow does not satisfy the slip-boundary condition that is assumed in the preceding topological classification theory for 2D flows [T. Sakajo and T. Yokoyama, *IMA J. Appl. Math.*, 83 (2018), pp. 380–411], [T. Sakajo and Y. Yokoyama, *Discrete Math. Algorithms Appl.*, 15 (2023), 2250143]. We thus establish a new topological classification theory and an algorithm suitable for blood flow with the moving boundary condition by introducing a degenerate singular point named n-bundled ss-saddle. Applying the theory to 2D blood flow patterns obtained by the visualization tools, we successfully identify vortical flow structures as topological vortex structures. This realizes a new image processing characterizing healthy blood flow patterns as well as inefficient patterns in diseased hearts.

Key words. flows with moving boundary, topological flow data analysis, vortex identification, blood flow visualization in the heart

MSC codes. 37C10, 58K45, 05C62, 37N10, 76Z05

DOI. 10.1137/22M1536923

1. Introduction.

Blood flow inside the heart contains several complex vortices at various phases of one cardiac cycle. Some of them are known to facilitate smooth blood flow ejection and filling. Disturbances in these vortices have been believed to cause inefficient flow and worsen heart diseases. Therefore, for detailed and profound inspection of the pathophysiology of the diseases, blood flow visualization has been developed based on noninvasive imaging modalities. The representative imaging tools are echocardiography vector flow mapping (VFM) and three-dimensional (3D) cine phase-contrast magnetic resonance imaging (four-dimensional (4D) flow MRI) [7]. They can describe blood flow details in the heart, even

*Received by the editors November 28, 2022; accepted for publication (in revised form) May 5, 2023; published electronically August 11, 2023.
https://doi.org/10.1137/22M1536923
Funding: The work of the first author was partially supported by the JST grant MIRAI JPMJMI22G1.
†Department of Mathematics, Kyoto University, Kyoto, 606-8224, Japan (sakajo@math.kyoto-u.ac.jp).
‡Department of Cardiovascular Surgery, Nagoya City University, and Cardio Flow Design Inc, Nagoya, Aichi 467-8602, Japan (keiichiitatani@gmail.com).

though it is highly unstable and turbulent due to repeated contraction and relaxation of the myocardium in a short period.

Although the heart has complex 3D flow in its complicated anatomy, the left ventricle (LV) is the main pump chamber with the highest power force for circulating the blood in the cardiovascular system. As the anatomy of the LV is plane-symmetric and pouch-shaped with aligned inlet and outlet valves that contact each other, the flow patterns in this plane have an essential physiological role in blood flow filling and ejection by optimizing the energy efficiency with a well-organized vortex [17]. In cardiovascular diseases, the disturbances of the LV vortex flow patterns have been expected to be one of the predictors of the prognosis of cardiac function which deteriorates with increased cardiac workload caused by the diseased turbulent flow [9, 16]. However, no clear definition of the vortical flow structures has been present for the blood flow stream so far. Hence, there are difficulties in utilizing these vortical flow structures in clinical imaging examination, such as size, center, and change over time.

Capturing those vortical flow structures of blood flows from the viewpoint of topology is a method to overcome the problems. For two-dimensional (2D) incompressible (Hamiltonian) and nonviscous flows, several investigations are classifying all possible streamline patterns topologically [2, 3, 11, 13, 15], but little attention has been paid to the identification of real flow data. In the meantime, based on the mathematical theory by Ma and Wang [13], a method of topological flow data analysis (TFDA) has been developed [25], where a unique symbolic graph expression, named COT (partially Cyclically Ordered rooted Tree) representation, is assigned to every topological streamline pattern generated by structurally stable 2D Hamiltonian flows. It has also been expected as practical as numerical pattern recognition for 2D incompressible and viscous flows [20], and has wide applications to practical problems in atmospheric science [23] and oceanography [19], for instance. The topological classification theory is recently extended for 2D compressible flows and a projection of 3D flows on a plane, and it is applied to some industrial problems [22]. In these preceding TFDA theories, 2D flows are assumed to satisfy the slip boundary condition. However, for some types of fluid flow in a bag-like pump such as the blood flow in the heart, the inflow/outflow from the valve yields a source/sink flow structure and moving boundaries push or pull the fluid, giving rise to instantaneous flow orbits that begin or end at the boundary. This sort of boundary condition should be taken into consideration so that TFDA theory can deal with blood flows in the LV.

The purpose of this paper is to construct a TFDA method suitable for 2D flows with a rapidly moving boundary such as those in the LV of the heart, thereby providing a topological image processing for echocardiography VFM to identify vortical flow structures in the heart. Section 2 is a guidance describing our motivation, needs in medical science, and the proposed TFDA method. Section 3 is a theoretical part providing a new topological classification theory for a class of 2D flows on the surface of a sphere with a degenerate singular orbit, called *a flow of finite type with an n-bundled ss-saddle.* We then show that a flow of finite type on an open disk with a transversal boundary condition, which is a mathematical model of 2D flows in the LV, is topologically equivalent to this class. In section 4, based on the classification theory, we provide an algorithm that assigns a discrete graph associated with a symbolic expression, i.e., COT representation, to every flow of finite type with an n-bundled ss-saddle. In section 5, based on the TFDA, we realize a new image processing identifying topological flow structures in 2D blood flow patterns in the LV. In particular, we show that vortical flow structures are

well identified as *topological vortex structures* using COT representations, thereby elucidating the difference between blood flows in the healthy heart and diseased hearts. The last section is a summary.

2. Guidance of the TFDA application to blood flow patterns in the heart.

2.1. 2D Blood flow patterns in the left ventricle anatomy of the heart. A heart ejects sufficient blood flow in each cardiac cycle with repeated contraction and relaxation. A heart with normal anatomy has two chambers named the right and left ventricles (RV and LV), which pump up blood to the lung and body, respectively. Figure 2.1(a) shows one cardiac cycle in the LV. The LV sucks blood in diastole after the mitral valve opens; then, after the filling ends, the mitral valve closes, and the LV contracts without changing its volume while the pressure inside it increases before the aortic valve opens (the isovolumic contraction period); and the LV pumps up blood in systole when the outlet aortic valve opens and the inlet mitral valve closes; then, after the aortic valve closes, the LV relaxes without changing its volume while the pressure decreases before the inlet mitral valve opens (the isovolumic relaxation period).

The inflow through the mitral valve should redirect and turn 180° inside the LV to form outflow, resulting in the formation of vortical flow structures [7]. Such vortical flow structures observed in the central plane of the LV are a 2D section of a torus-shaped 3D vortical flow named "vortex ring" [10]. The shape of the LV is anatomically plane-symmetric in the long-axis plane which passes through the centerline of the aortic and mitral valves, and 2D flow patterns in this long-axis plane play an essential physiological role inside the LV chamber. Hence, we pay attention to these 2D flow patterns. We assume that the flow pattern consists of orbits constructed from an instantaneous vector field, called streamlines in the field of medical blood flow imaging. Let us note that, as blood flow inside the heart changes its pattern drastically within one cardiac cycle, the streamlines in an arbitrarily fixed time do not coincide with blood cell particle paths or trajectories.

2.2. Blood flow imaging modalities with echocardiography and cardiac MRI. In medical imaging examinations, echocardiography and cardiac MRI can visualize blood flow inside the heart chamber. See Figure 2.1(b). Echocardiography VFM provides 2D blood flow velocity vector distribution [8] in an LV symmetrical long-axis plane based on the color Doppler data. In cardiac MRI, since phase-contrast MRI (PC-MRI) detects blood flow velocity distribution in the arbitrary direction of the magnetic gradient, a combination of PC-MRI images in three directions makes it possible to reconstruct a 3D blood flow velocity vector with pulsatile motion (4D flow MRI). After the reconstruction of the 3D flow vector or streamline, an LV long-axis cross-section is cut, and a 2D projection of instantaneous flow streamline is obtained [7].

Figure 2.1(c) shows a time series of 2D flow patterns in one cardiac cycle obtained by echocardiography VFM. The previous imaging research results confirmed that the 2D flow stream scanned in the echocardiography VFM has almost the same pattern as that obtained from the plane projection map of the 3D flow stream measured by 4D flow MRI [6, 17]. In each panel, the apical portion of the LV is on the top side, while the two valves are located at the basal portion. In diastole and systole, typical vortical flow patterns appear in the LV when accelerated blood flow ejects from and fills into the LV through the valves, respectively.

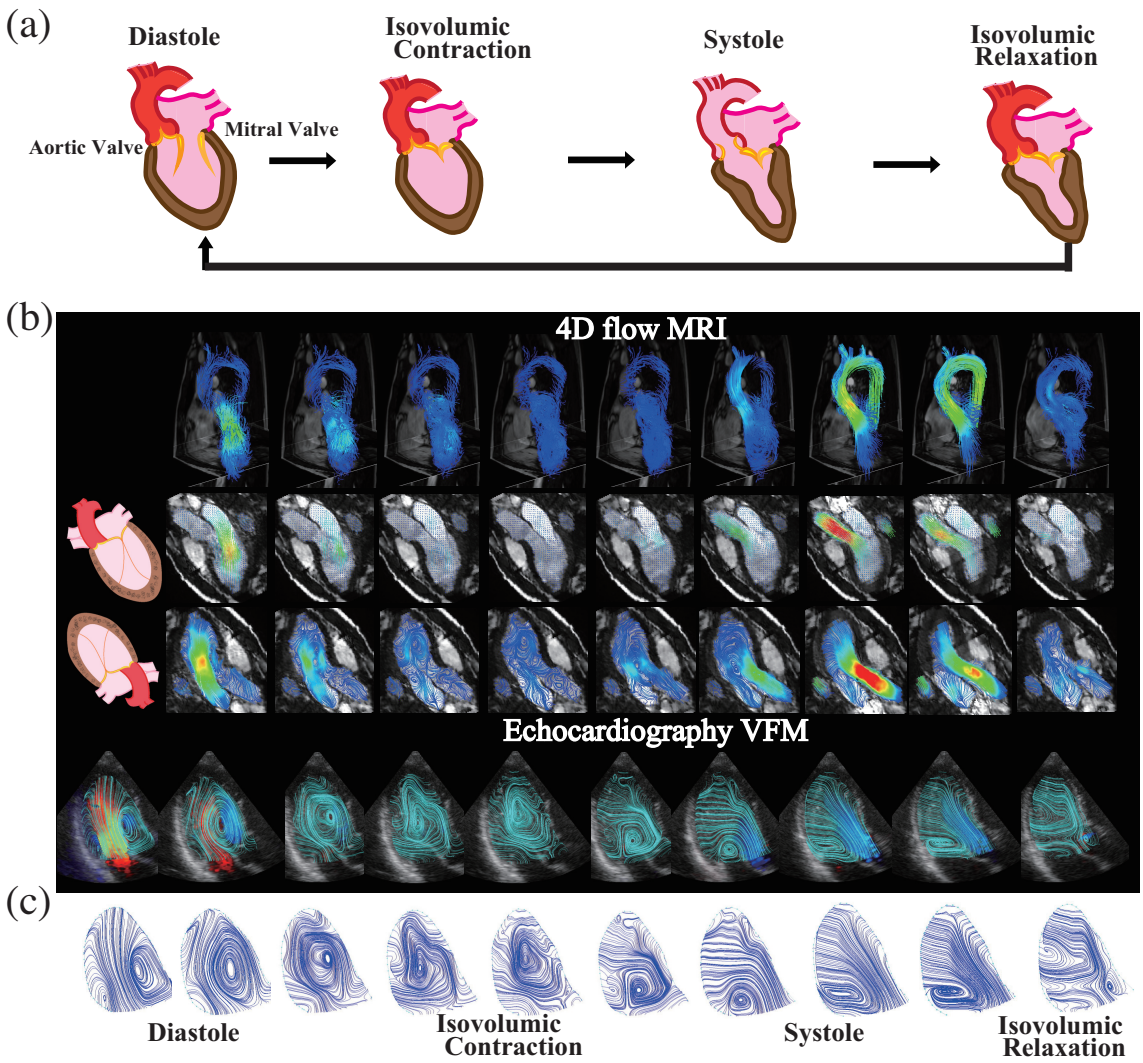

Figure 2.1. (a) *Cardiac cycle in the LV.* (b) *Blood flow imaging with 4D flow MRI and echocardiography VFM. Blood pressure changes with the motion of the LV wall and the valves.* (c) *Vortical flow patterns in the central cross-sectional plane of the LV obtained by echocardiography VFM.*

They are frequently observed for healthy hearts in clinical practice. Several other structures such as the mitral valve chords inside the LV can be physical boundaries anatomically, but they are so small and thin that flow imaging by echocardiography VFM or cardiac MRI does not have sufficient resolution to detect these structures. Hence, the 2D blood flows in the LV are regarded as flows in an open disk.

2.3. Medical needs for the extraction of the vortex structure in the LV. Many reports in medical sciences have revealed the characteristic behavior of the LV vortex in heart diseases or in the postoperative state of cardiac surgeries. For example, the duration of the main vortex in the LV during systole was related to the heart failure state of cardiomyopathy, and

the vortex size was reduced in successful medication therapy [16]. The reduced persistence of vortex during systole was reported in successful cardiac resynchronization therapy with a pacemaker for heart failure [9]. Even the direction of the vortex can be easily changed when the inlet mitral valve is replaced with an artificial valve [1]. Therefore, so many hemodynamic parameters, not limited to those derived from blood flow imaging such as classical chamber ejection fraction or heart wall motion tracking, have been developed in imaging in cardiology. Among them, Cho et al. [4] suggested the importance of vorticity before the LV contraction in the evaluation of the cardiac function based on the machine learning results on the clinical imaging data on echocardiography. In these reports, vortical flows in the LV have been handled empirically without a clear definition of "vortex." However, because the vortex seems to play an essential role in cardiac function, especially in heart failure patients, its quantification is inevitable, and for this purpose, accurate identification of the shape, size, and position of vortex structures is required. This is the motivation in medical science, leading to a need for a definite definition of the vortex structure.

2.4. TFDA for flow pattern images in the LV. Figure 2.2(a) is an echocardiography image of the LV of a healthy heart. Background color Doppler describes the flow direction toward (blue) or apart from (red) the probe attached to the body surface. For this image, VFM visualizes a flow vector distribution of the blood flow inside the LV as in Figure 2.2(b). Because of the limitations in resolution, information on the vortex structure such as the positions of the vortex centers, and/or their attractors is not apparent. Hence, VFM further constructs streamlines from the vector distribution with interpolated and smoothed noisy measurement data such as Figure 2.2(c), in which we can find a rotational flow in the LV, but it is still unclear which area to be identified as the vortex flow structure in the LV.

TFDA identifies such vortex structures from the viewpoint of topology. Let us first extract singular points such as centers, sources/sinks, saddle points, and their connecting orbits from the streamlines as in Figure 2.2(d). We then construct a "skeleton" image, called *the ss-saddle connection diagram,* consisting of the singular points and the connecting orbits. See Figure 2.2(e). By applying the TFDA theory in section 3.3 and the algorithm in section 4.4, the topological information of the ss-saddle connection diagram is uniquely expressed with a tree (graph) structure and its symbolic representation, called *COT representation.* For this example, the tree structure (COT) is given in Figure 4.5(e) associated with the COT representation (4.5). With COT representations, one can identify the difference between the flow patterns in the LV of healthy hearts and diseased hearts as in section 5. Moreover, in order to describe the physiological or pathological role of the vortex, the vortex flow domain and its relation to the other blood flow domains should be accurately determined. The COT representation yields the decomposition of the flow domain as in Figure 2.2(f), in which the red domain is identified as a topological vortex structure. We thus quantize the domain to understand the role of the vortex in the LV. In this way, the TFDA is suitable for this process to meet medical needs.

Theoretically, the preceding TFDA theory for the flow of finite type [22] is not applicable to the blood flows in the LV as it is: The flow domain inside the LV is regarded as topologically equivalent to the open disk without inner boundaries, say Ω_{LV}, and the flow structures inside the disk domain consist of singular orbits, limit circuits, and their connecting orbits

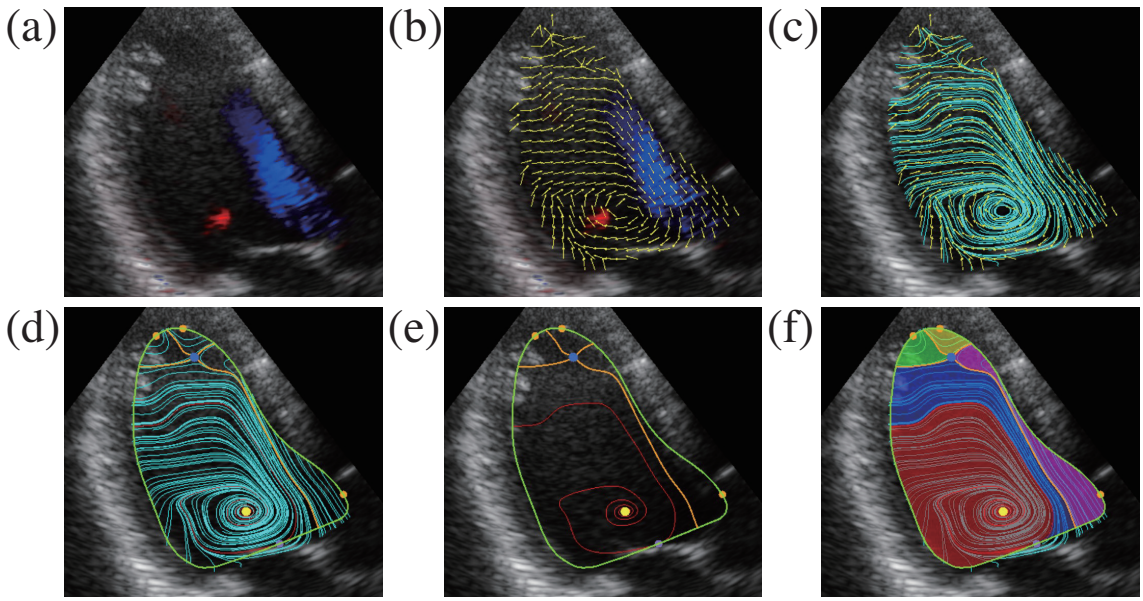

Figure 2.2. (a) *Color Doppler flow mapping in the LV with echocardiography.* (b) *Flow vectors with echocardiography VFM.* (c) *Flow streamlines reconstructed by the vectors obtained with echocardiography VFM.* (d) *Flow orbit structures and singularities based on streamlines.* (e) *Singular points and their connecting orbits form an ss-saddle connection diagram.* (f) *Decomposition of the flow region brought by the TFDA.*

appearing in the flow of finite type. However, the slip boundary condition required by the theory is not satisfied with the flows in the LV. Indeed, they do not slip the chamber or vessel wall boundaries but interact with each other, resulting in forming characteristic pulsatile motion of instantaneous flow patterns. As observed in Figure 2.1(c), in diastole, ventricular muscle relaxation causes chamber dilatation with the sucking force of blood, resulting in inflow through the mitral valve, and again mechanical equilibrium in the contact surface is maintained between blood pressure and muscle sucking force. The ventricular muscle boundary in this situation is the sink of the flow inside the heart, and the mitral valve or inflow is the source of the chamber flow. On the other hand, in systole, as also shown in Figure 2.1(c), ventricular muscle contraction pushes the blood, resulting in ejection flow from the ventricular chamber to the outlet (opening the aortic valve), and the contact surface or boundary between muscle and blood maintains the mechanical equilibrium of blood pressure and the contractile muscle force. The ventricular muscle boundary in this situation is the source of the flow inside the heart, and the aortic valve or outflow is the sink of the chamber flow. Hence, it is natural to assume the transversal boundary condition of the flow on $\partial\Omega_{LV}$. To resolve the boundary condition problem, we convert the flow in the disk Ω_{LV} into a flow on the surface $S \subseteq \mathbb{S}^2$ by "gluing" the boundary $\partial\Omega_{LV}$ into a point as explained in section 3.4. At the glued point, we then set a degenerate singular orbit, called an *n-bundled ss-saddle* as constructed in Figure 3.2(a). As a result, the transversal flows at the moving boundary of the disk are expressed by this static degenerate flow structure of sources and sinks on the sphere. We thus establish a new TFDA theory for the flow of finite type with an n-bundled ss-saddle in section 3, and provide an algorithm suitable for blood flows in the LV in section 4. In

section 5, we show the application of the proposed TFDA method to actual echocardiography images of healthy and diseased hearts.

3. Flow orbit structures and topological classification theory.

3.1. Preliminaries. Let us recall some mathematical notions in the theory of dynamical systems. Let $v\colon \mathbb{R}\times S\to S$ denote a continuous $\mathbb{R}$-action on a spherical surface $S\subseteq\mathbb{S}^2$ without boundaries, which we call a flow on S. By introducing a map $v_t : S\to S$ by $v_t := v(t,\cdot)$ for any $t\in\mathbb{R}$, an orbit starting from $x\in S$ is given by

$$O(x) := \{v_t(x)\in S \,|\, t\in\mathbb{R}\}.$$

For any smooth vector field $u(x)$, a unique solution $\varphi(t;x)$ of the initial value problem $\dot\varphi = u(\varphi(t))$ and $\varphi(0)=x\in S$ gives rise to a flow on S by $v_t(x):=\varphi(t;x)$.

A point $x\in S$ is a *singular* orbit if $x=v_t(x)$ for any $t\in\mathbb{R}$, i.e., $O(x)=\{x\}$. An orbit $O(x)$ is said to be *periodic* if there exists $T>0$ such that $x=v_T(x)$ and $x\neq v_t(x)$ for any $t\in(0,T)$. We say an orbit is *nonclosed* if it is neither singular nor periodic. The ω-limit (resp., α-limit) set of $x\in S$ is defined by $\omega(x) := \cap_{n\in\mathbb{R}}\overline{\{v_t(x)\,|\,t>n\}}$ (resp., $\alpha(x) := \cap_{n\in\mathbb{R}}\overline{\{v_t(x)\,|\,t<n\}}$). A *separatrix* is a regular orbit whose α-limit or ω-limit set is a singular orbit.

Let u be a vector field on a compact smooth manifold M with isolated N singular orbits and solid boundaries satisfying the slip boundary condition. Then, orbit structures generated by u can be complicated under the following global topological constraint on u:

$$\sum_{i=1}^{N}\mathrm{ind}_{x_i}(u)=\chi(M), \tag{3.1}$$

where $\chi(M)$ is the Euler characteristic of M, $\mathrm{ind}_{x_i}(u)$ denotes the index of u at the singular orbit $x_i\in M$ for $i=1,\dots,N$. This is a generalization of the Poincaré–Hopf theorem for vector fields on a compact manifold [12]. The Euler characteristics of the spherical surface $\mathbb{S}^2$ without boundaries is given by $\chi(\mathbb{S}^2)=2$.

3.2. Topological flow components.

3.2.1. Zero-dimensional flow components. We introduce nondegenerate singular orbits and a special degenerate singular orbit as zero-dimensional orbits. Since no boundary is contained in the spherical surface S, every nondegenerate singular orbit is either a center, a saddle, a source, or a sink as shown in Figure 3.1.

Definition 3.1. *A point $x\in S$ is a sink (resp., a source), if there is a neighborhood U of x such that $\omega(y)=\{x\}$ (resp., $\alpha(y)=\{x\}$) for any $y\in U$. A point $x\in S$ is a center, if there is a neighborhood U of x such that $U-\{x\}$ is filled with periodic orbits. A saddle is an isolated singular orbit with exactly four separatrices.*

Note that the index of a center, a source, or a source is 1, and that of a saddle is -1.

We now construct a degenerate singular orbit as follows. See Figure 3.2(a). Let us consider an open neighborhood of a point $x\in S$ containing n (≥ 1) saddles with $4n$ saddle separatrices that intersect ∂U transversely. Then, U is divided into $3n+1$ disjoint open domains by these separatrices. In addition, we put a center at each disjoint domain whose boundary

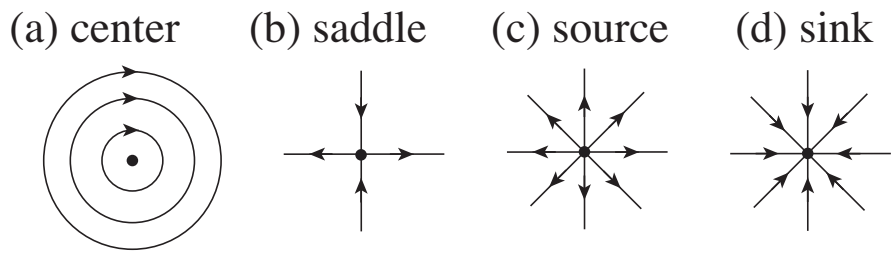

Figure 3.1. *Nondegenerate singular orbits.* (a) *A center.* (b) *A saddle.* (c) *A source.* (d) *A sink.*

contains only one saddle. Let us notice that there are $2n+2$ such domains in U containing a center. By collapsing U into the point x, we obtain a degenerate point, which is referred to as an n-bundled source-sink saddle (n-*bundled ss-saddle* in short). Since we collapse these $2n+2$ centers and n saddles into one point, the index of this degenerate singular orbit is $2n+2+(-n)=n+2$.

We observe orbit structures in the neighborhood of the degenerate point. Let us consider a flow on the open domain U in which n saddles are arranged in a row and $2n+2$ centers are placed as shown in Figure 3.2(a). By collapsing the centers and the saddles to the point x, we obtain an n-bundled ss-saddle to which $4n$ saddle separatrices converge. Then, orbits in a subdomain of U with a center are reduced to orbits connecting the degenerate point by the collapse. It yields a source-sink wedge domain, called *an elliptic sector* [18]. On the other hand, by the collapse, a subdomain without a center is divided into two wedge domains where orbits converge to and emanate from the degenerate point. These wedge regions are referred to as *parabolic sectors* [18]. Hence, orbit structures in the neighborhood of an n-bundled ss-saddle comprise elliptic and parabolic sectors.

Figure 3.2(b) shows four elliptic sectors near the 1-bundled ss-saddle. The 2-bundled ss-saddle is associated with four elliptic sectors and two parabolic sectors as shown in Figure 3.2(c). For $n \geq 3$, the arrangement of n saddles with $4n$ saddle separatrices in U is not unique. For instance, when $n=3$, we have two topologically different arrangements of three saddles as in Figure 3.2(d). By the collapse, we obtain the 3-bundled ss-saddles having eight elliptic sectors and four parabolic sectors. While the count of sectors remains the same, the cyclic arrangement of these sectors is different.

A dipole singular orbit in Figure 3.2(e) is formally identified with an n-bundled ss-saddle with $n=0$. As a matter of fact, the degenerate singular orbit is obtained by putting $2\cdot 0+2$ centers and collapsing to a point. We remark that the flow in the neighborhood of n-bundled saddles ($n \geq 2$) is different from the flow generated by the complex potential with the pole singularities $1/z^{2n+2}$ of order $n+2$, whereas 0-/1-bundled saddle is locally topologically equivalent to that of the poles of order two or four in its neighborhood.

3.2.2. One-dimensional flow components. For a mapping from a circle $f:\mathbb{S}^1 \to S$, when its image is a point, it is nothing but a singular orbit. When f is immersion, the image is called a *circuit.* Any circuit is either a *cycle,* which is a periodic orbit as in Figure 3.3(a), or a *nontrivial circuit,* which is a 1D connected subset composed of separatrices and singular orbits as shown in Figure 3.3(b).

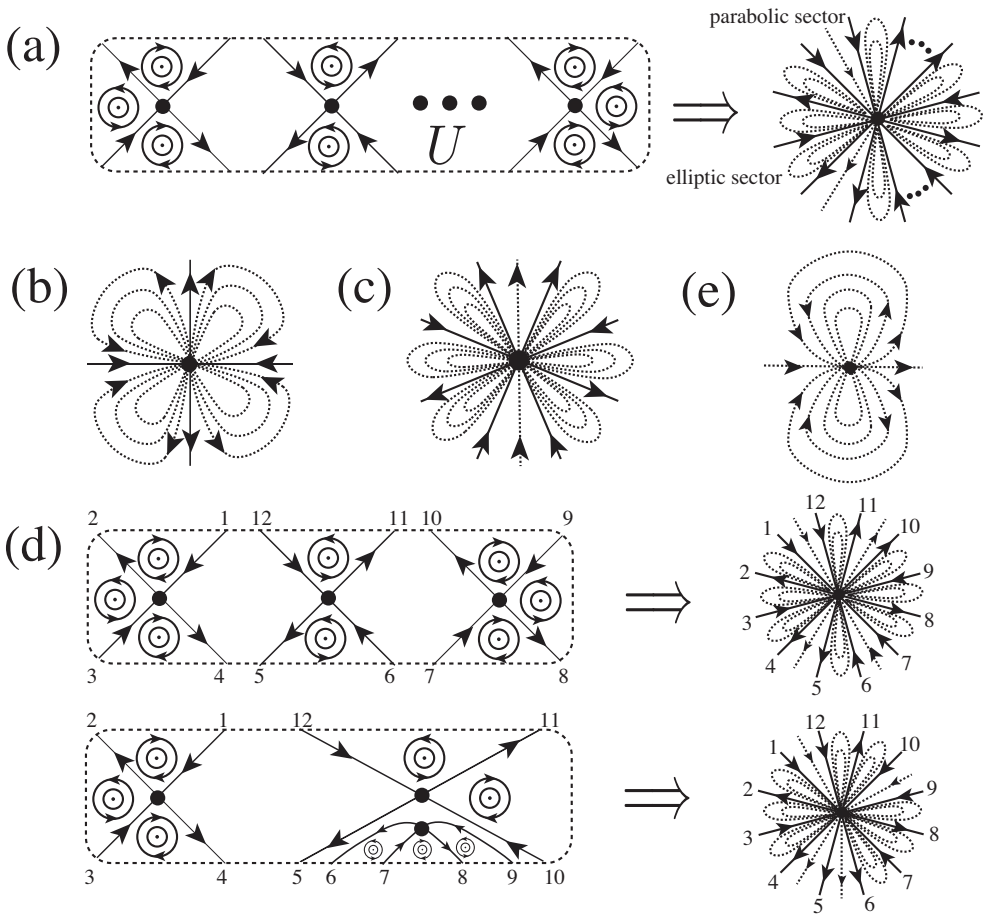

Figure 3.2. *Degenerate n-bundled ss-saddles.* (a) *A schematic explaining how to construct the degenerate singular orbit.* (b) *Orbit structure in the neighborhood of a* 1*-bundled ss-saddle.* (c) *Orbit structure in the neighborhood of a* 2*-bundled ss-saddle.* (d) *Orbit structures in the neighborhood of two different* 3*-bundled ss-saddles.* (e) *Orbit structure in the neighborhood of a* 0*-bundled ss-saddle. In each panel, solid lines represent separatrices connecting to the degenerate singular orbit and dotted lines are nonclosed orbits connecting the degenerate singular orbit as their* α*-limit set or* ω*-limit set.*

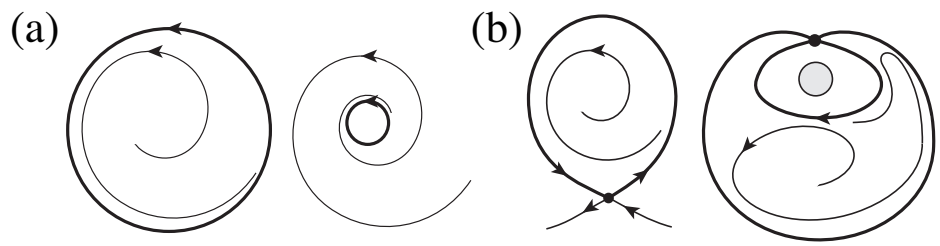

Figure 3.3. *Examples of limit circuits.* (a) *Limit cycles.* (b) *Nontrivial limit circuits. They are drawn as thick black curves and filled circles.*

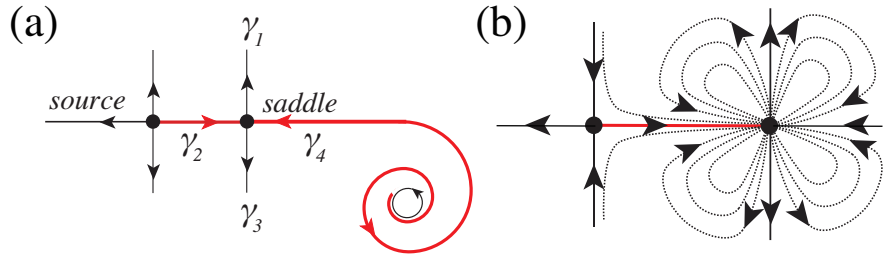

Figure 3.4. *Examples of ss-components and ss-separatrices. All ss-separatrices are drawn as red solid lines.* (a) *An ss-separatrix connecting a source and a saddle (left), and an ss-separatrix between a saddle and a limit cycle (right). The saddle is slidable.* (b) *An ss-saddle separatrix connecting a saddle and a* 1*-bundled ss-saddle.*

Definition 3.2. *A limit circuit γ is a circuit satisfying either $\alpha(x)=\gamma$ or $\omega(x)=\gamma$ for some point $x\notin\gamma$. In addition, it is called attracting (resp., repelling), if there is an open annulus $\mathbb{A}$ such that one boundary of $\mathbb{A}$ is γ and $\mathbb{A}\subseteq W^s(\gamma)$ (resp., $\mathbb{A}\subseteq W^u(\gamma)$), where $W^s(\gamma)$ (resp., $W^u(\gamma)$) denotes the stable (resp., the unstable) manifold of γ.*

By definition, any limit circuit should be attracting or repelling from at least outside or inside.

Definition 3.3. *A saddle separatrix is a separatrix whose α-limit and ω-limit sets are saddles. In particular, when a saddle separatrix connects the same saddle, it is called self-connected.*

An *ss-component* is either a sink, a source, a limit circuit, or an n-bundled ss-saddle. A 1D orbit connecting a saddle and an ss-component is called an *ss-separatrix.* See Figure 3.4. We introduce another special orbit structure containing ss-separatrices.

Definition 3.4. *Let γ_1, γ_2, γ_3, and γ_4 denote four separatrices of a saddle x with $\alpha(\gamma_1)=\alpha(\gamma_3)=\omega(\gamma_2)=\omega(\gamma_4)=x$. If $\alpha(\gamma_2)$ (resp., $\omega(\gamma_1)$) is a source (resp., a sink) which is not $\alpha(\gamma_4)$ (resp., $\omega(\gamma_3)$), the saddle x is then called slidable. See Figure* 3.4(a).

The union of centers, saddles, saddle separatrices, ss-components, and ss-separatrices generated by the flow v on S is referred to as the *ss-saddle connection diagram,* denoted by $D_{ss}(v)$.

3.2.3. Two-dimensional flow components. These are open flow domains filled with infinitely many nonclosed/periodic orbits, which are defined in terms of orbit space as follows.

Definition 3.5. *Let $T\subset S$ denote a union of orbits. The orbit space is defined as a quotient set $T/\sim$, where the equivalence relation $\sim$ is defined by $x\sim y$ for $x,y\in T$, if $O(x)=O(y)$.*

Definition 3.6. *A uniform flow box is an open flow box filled with nonclosed orbits whose orbit space is an open interval. A transverse annulus is an open annulus filled with nonclosed orbits whose orbit space is a circle. A periodic annulus is an open annulus filled with periodic orbits whose orbit space is an open interval. See Figure* 3.5(a)–(c).

3.3. Topological classification theory. Let us clarify the mathematical object considered in the present theory.

Definition 3.7. *Let $S\subseteq\mathbb{S}^2$ denote a spherical surface without solid boundaries. A flow on S is called a flow of finite type with an n-bundled ss-saddle, if it satisfies* (1) *all singular orbits*

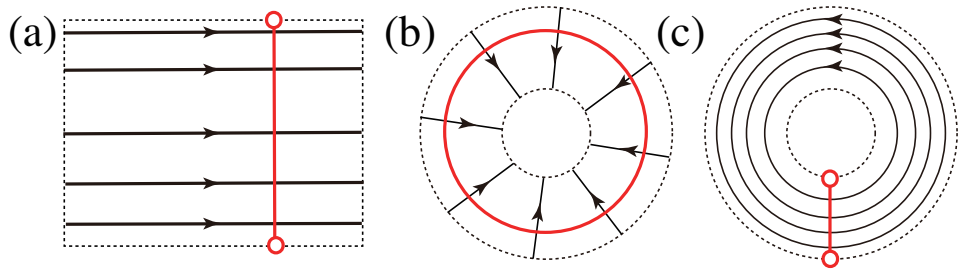

Figure 3.5. *Two-dimensional flow components. Orbits filling the domains are drawn as black solid lines with arrows, while their orbit spaces are shown in red.* (a) *A trivial flow box: an open box whose orbit space is an open interval.* (b) *A transverse annulus: an open annulus whose orbit space is a circle.* (c) *A periodic annuls: an open annulus whose orbit space is an open interval.*

are non-degenerate except the n-bundled ss-saddle; (2) *the number of limit cycles is finite;* (3) *all saddle separatrices between saddles are self-connected.*

The first restriction yields that all singular orbits are isolated and finite. The second one excludes the accumulation of limit cycles. By the third restriction, we exclude the existence of orbits connecting different saddles, i.e., heteroclinic connections, which cannot persist in practical flow data due to errors and noises.

The following is a generalization of Poincaré–Bendixson lemma, describing the α-limit and the ω-limit sets in the flow of finite type with an n-bundled ss-saddle.

Lemma 3.8. *The ω-limit set (resp., the α-limit set) of a point in the flow of finite type with an n-bundled ss-saddle is one of the following:* (1) *a saddle;* (2) *a sink (resp., a source);* (3) *an attracting (resp., repelling) limit cycle;* (4) *an attracting (resp., repelling) nontrivial limit circuit;* (5) *an n-bundled ss-saddle.*

Proof. The proof is based on the same lemma for the flow of finite type with no degenerate singular orbits in [22]. Since no solid boundary exists in the flow domain, we exclude saddles, sinks, and sources on the boundary. But we need to add an n-bundled ss-saddle as an element of the ω-limit and α-limit sets by definition. ∎

This lemma indicates that saddle separatrices generated by the flow of finite type with an n-bundled ss-saddle consist of self-connected saddle separatrices and ss-separatrices in the ss-saddle connection diagram $D_{ss}(v)$.

In the meantime, according to a general theory in [14], any orbit of the flow v on the spherical surface $S \subseteq \mathbb{S}^2$ is *proper,* meaning that there exists a neighborhood of the orbit in which it becomes a closed set. The set of proper obits is decomposed into the sets of singular orbits $\mathrm{Sing}(v)$, the union of periodic orbits $\mathrm{Per}(v)$ and the union of nonclosed orbits $\mathrm{P}(v)$. Then, we define the set of border orbits, say $\mathrm{Bd}(v)$, for the flow of finite type v with an n-bundled ss-saddle.

Definition 3.9. *The set of border orbits $\mathrm{Bd}^h(v)$ of the flow of finite type v with an n-bundled ss-saddle on the spherical surface S without boundaries is given by*

$$\mathrm{Bd}^h(v) := \mathrm{Sing}(v) \cup \mathrm{P}^h_{\mathrm{sep}}(v) \cup \partial \mathrm{P}(v) \cup \partial \mathrm{Per}(v),$$

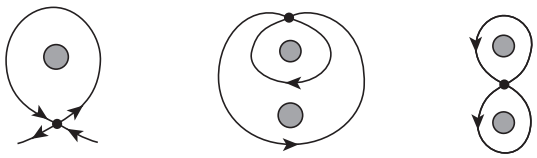

Figure 3.6. *Nontrivial limit circuits generated by the flow of finite type with an n-bundled ss-saddle.*

where $\mathrm{P}^h_{\mathrm{sep}}(v)$, $\partial\mathrm{P}(v)$, *and* $\partial\mathrm{Per}(v)$ *denote the union of saddle separatrices and ss-separatrices, the boundary set of nonclosed orbits, and the boundary set of periodic orbits, respectively.*

Centers, saddles, sources, sinks and an n-bundled ss-saddle in $D_{ss}(v)$ are elements of $\mathrm{Sing}(v)$. Self-connected saddle separatrices and ss-separatrices are elements of $\mathrm{P}^h_{\mathrm{sep}}(v)$. Regarding limit circuits, when they are attracting and/or repelling from both sides, they are elements of $\partial\mathrm{P}(v)$. On the other hand, when a limit circuit is attracting or repelling from one side and periodic orbits are filled on the other side, it is an element of $\partial\mathrm{Per}(v) \cap \partial\mathrm{P}(v)$. On the other hand, elements in $\mathrm{Sing}(v)$ and $\mathrm{P}^h_{\mathrm{sep}}(v)$ are orbits in $D_{ss}(v)$, and an element in $\partial\mathrm{P}(v)$ is either a limit circuit, an ss-separatrix, a saddle, or an ss-component. Orbit in $\partial\mathrm{Per}(v)$ is a limit circuit where nonclosed orbits converge only from one side. Hence, $D_{ss}(v)$ is equivalent to $\mathrm{Bd}^h(v)$.

Let us here note the difference between $\mathrm{Bd}^h(v)$ and $\mathrm{Bd}(v)$ for the flow of finite type considered in Sakajo and Yokoyama [22]. First, the border set $\mathrm{Bd}^h(v)$ does not contain periodic orbits along boundaries since no boundary exists in S. Second, the n-bundled ss-saddle is an additional element of $\mathrm{Sing}(v)$, but no saddles on ∂S exists as $\mathrm{Sing}(v)$ in $\mathrm{Bd}^h(v)$. Last, $\mathrm{P}^h_{\mathrm{sep}}(v)$ contains new ss-separatrices to the n-bundled ss-saddle as in Figure 3.4(b).

Since the flow of finite type with an n-bundled ss-saddle on S is an extension of the flow of finite type without saddles on ∂S, it inherits similar properties to those of the flow of finite type. For instance, any nontrivial limit circuit in $\mathrm{Bd}^h(v)$ is either a saddle with one self-connected saddle separatrix or a saddle connected by two self-connected saddle separatrices as shown in Figure 3.6. We now state the topological structure theorem, in which the complement $(\mathrm{Bd}^h(v))^c = S - \mathrm{Bd}^h(v)$ consists of the three 2D domains in Figure 3.5. The original proof is given in Yokoyama [24] with a general mathematical framework.

Theorem 3.10. *For any flow of finite type with an n-bundled ss-saddle on a spherical surface S without boundaries, each connected component of $(\mathrm{Bd}^h(v))^c$ is either a uniform flow box, a transverse annulus, or a periodic annulus.*

Proof. For 2D flow domains separated by the border orbits in the interior of S, the classification is the same as shown in the topological structure theorem for flows of finite type on S [22, 24] without saddles on the boundary ∂S or the degenerate singular orbit. Hence, it is sufficient to consider the classification of the orbit structures separated by ss-separatrices connecting to the n-bundled ss-saddle. The 2D domain in the neighborhood of the ss-separatrices becomes a uniform flow box. The proof is finished. ∎

3.4. The flow of finite type in a disk with a transversal boundary condition. Let us consider a vector field on an open disk Ω without inner boundaries. We then assume that orbits generated by the vector field cross the boundary transversally almost everywhere on

$\partial\Omega$. Moreover, there are neither orbits of higher-order tangency crossing the boundary, nor points of inner tangency where orbits are tangent to the boundary from inside. We now show that the flow of finite type on Ω with this transversal boundary condition is topologically equivalent to the flow of finite type with an n-bundled ss-saddle on a spherical surface $S \subseteq \mathbb{S}^2$ without boundaries.

To transform orbits in Ω into those in S, we introduce the following equivalence relation between two points $x, x' \in \overline{\Omega}$:

$$\forall x, x' \in \overline{\Omega}, \quad x \sim x' \Longleftrightarrow x, x' \in \partial\Omega, \tag{3.2}$$

where $\overline{\Omega}$ denotes the closure of Ω. By gluing all points on $\partial\Omega$ at one point, say $\{\infty\}$, by this equivalence relation, the flow domain $\Omega/\sim$ becomes a punctured spherical surface $S = \mathbb{S}^2 \setminus \{\infty\}$. We then make the vector field smooth so that the glued point $\{\infty\}$ becomes a singular orbit. Such smoothing is possible by multiplying a smooth bump function around $\{\infty\}$ as discussed by Gutierrez [5]. Consequently, all orbits intersecting the boundary $\partial\Omega$ converge to the singular orbit at $\{\infty\}$.

Suppose that $n \geq 1$ saddles exist in Ω and their $4n$ saddle separatrices cross the boundary $\partial\Omega$ transversely. We then find that the singular orbit at $\{\infty\}$ becomes an n-bundled ss-saddle: The Poincaré–Hopf index equality (3.1) for vector fields on S implies that the index of the singular orbit becomes $\chi(\mathbb{S}^2) - (-n) = n + 2$. In addition, since we assume no points of inner tangency exist on $\partial\Omega$, the orbit structure in the neighborhood of the degenerate singular orbit is classified into two cases. First, orbits are in a domain enclosed by the boundary of the disk, a saddle, and its two saddle separatrices. Second, orbits are penetrating in a flow box between four saddle separatrices of two different saddles. Creating the degenerate singular orbit by gluing the boundary and smoothing the vector field, we obtain an elliptic sector in the former case and parabolic sectors in the latter case. Hence, orbit structures in the neighborhood of the degenerate singular orbit comprise elliptic and parabolic sectors, which means that the singular orbit is an n-bundled ss-saddle.

In the meantime, when there contains no saddle in Ω, we have two kinds of orbit structures in Ω crossing the boundary. One orbit structure is the flow on Ω containing a source (resp., a sink) orbit structure. By gluing the boundary, it gives rise to a flow on the surface S with a sink (resp., a source) at $\{\infty\}$. Then, the vector field is regular on S. Another orbit structure is a uniform flow box. By the gluing, we obtain a dipole singular orbit at $\{\infty\}$ as shown in Figure 3.2(e). The singular orbit is identified with a 0-bundled ss-saddle.

In conclusion, the n-bundled ss-saddle appears by gluing the boundary, and the gluing operation does not change the properties of the flow on the interior of Ω, satisfying the conditions of Definition 3.7. Hence, the flow of finite type with an n-bundled ss-saddle on a spherical surface is equivalent to that on an open disk with a transversal boundary condition, to which the topological classification theorem (Theorem 3.10) is applicable.

Note that gluing the boundary without inner tangencies implies an n-bundled ss-saddle, which means no hyperbolic sectors, and thus no Reeb components are supposed to appear in Ω. However, in the actual flow pattern in the LV by echocardiography VFM, only a finite number of isolated inner tangencies can appear on $\partial\Omega$, which requires a certain image processing modification to these points to be theoretically consistent as explained in section 3.5.

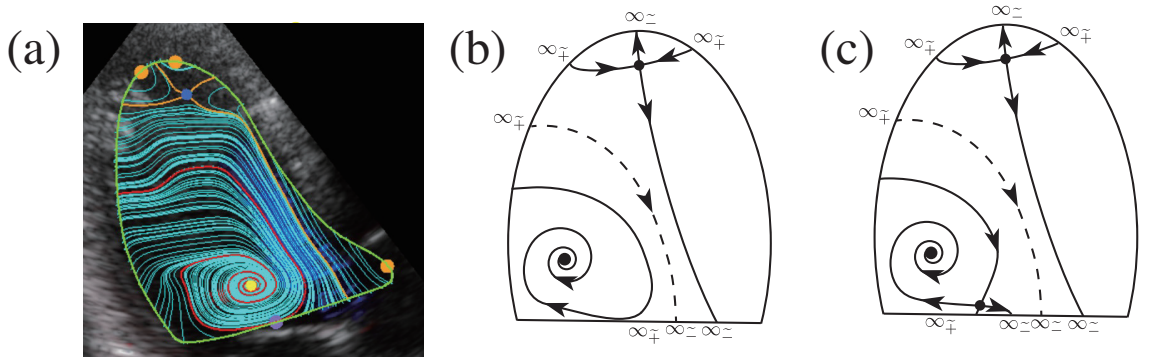

Figure 3.7. *Topological preconditioning for an ss-saddle connection diagram.* (a) *Border orbis in the ss-saddle connection diagram $D_{ss}(v)$ extracted from an original echocardiography VFM image. The blue point is a saddle, the yellow one is a sink, the purple one is a point of inner tangency and the orange one are points of outer tangency.* (b) *A schematic of the ss-saddle connection diagram constructed from panel* (a). *The point of inner tangency appears at the bottom of the boundary.* (c) *A schematic of the ss-saddle connection diagram after the topological preconditioning, making the transversal boundary condition satisfied.*

3.5. Mathematical model of flow patterns in the LV of the heart. As we see in section 2.2, the flow domain brought by the echocardiography VFM or cardiac MRI is topologically equivalent to the open disk without inner boundaries Ω_{LV}. We may regard that all singular orbits in Ω_{LV} are nondegenerate, the number of limit cycles is finite and saddle separatrices are self-connected, since the resolution of these modalities is limited, and it thus captures the finite number of robust orbit structures when the reconstructed orbits are based on interpolated and smoothed flow velocity measurement data. For example, Figure 3.7(a) shows several flow orbits, in which a saddle is shown as a blue point at the apical portion, a clockwise sink as a yellow point at the basal portion, and three points of outer tangency as orange points on the boundary $\partial\Omega_{LV}$. In order to model the flows in Ω_{LV} as the flow of finite type with an n-bundled ss-saddle on $S \subseteq \mathbb{S}^2$ from the viewpoint of section 3.4, the transversal boundary condition must be satisfied. However, in actual blood flow patterns inside the LV, a few isolated inner tangencies appear on the boundary when the rotating vortex flow structure exists. Indeed, in Figure 3.7(a), we observe a point of inner tangency as a purple point at the bottom of the boundary. Figure 3.7(b) is a schematic of the ss-saddle connection diagram of Figure 3.7(a), to which the TFDA theory is not applicable due to the existence of the point of inner tangency. As a remedy to this phenomenon, we replace the point of inner tangency with a slidable saddle, where one of its ss-separatrices leads to the sink structure and the other one crosses the LV boundary transversely as shown in Figure 3.7(c). As a result, the flow satisfies the transversal boundary condition. This process is implemented successfully in the practical image processing as shown in Figure 3.7(a), where trajectories with the inner tangency are detected as red curves and they are regarded as ss-saddle separatrices associated with the replaced slidable saddle. We call this operation of removing inner tangencies *topological preconditioning.* Hence, it is natural to assume that the flow in the 2D section of the LV after the topological preconditioning is modeled as the flow of finite type in the disk Ω_{LV} with the transversal boundary condition, to which the classification theory is now applicable.

Table 4.1

Classfication of all orbit structures and COT symbols used to describe tree representations of the flows of finite type with an n-bundled ss-saddle.

Class	Notation	Orbit structures in the class	Note
class–b_+	$\square_{b_+}$	$b_{\widetilde{\pm}}, b_+$	2D orbit structures
class–b_-	$\square_{b_-}$	$b_{\widetilde{\pm}}, b_-$	2D orbit structures
class–$b_{\widetilde{\pm}}$	$\square_{b_{\widetilde{\pm}}}$	$b_{\widetilde{\pm}}$	2D orbit structures
class–$\widetilde{+}$	$\square_{\widetilde{+}}$	$p_\pm, b_{\pm\pm}, b_{\pm\mp}, q_\pm, a_{\widetilde{+}}, \sigma_{\widetilde{+}\pm}\sigma_{\widetilde{+}0}$	source orbit structures
class–$\widetilde{-}$	$\square_{\widetilde{-}}$	$p_\pm, b_{\pm\pm}, b_{\pm\mp}, q_\pm, a_{\widetilde{-}}, \sigma_{\widetilde{-}\pm}, \sigma_{\widetilde{-}0}$	sink orbit structures
class–α_+	$\square_{\alpha_+}$	$p_{\widetilde{+}}, b_{++}, b_{+-}, q_+, \sigma_+$	Embedded only in b_+
class–α_-	$\square_{\alpha_-}$	$p_{\widetilde{-}}, b_{-+}, b_{--}, q_-, \sigma_-$	Embedded only in b_-
class–a	$\square_a$	$a_\pm$	
class–$a_{\widetilde{-}}$	$\square_{a_{\widetilde{-}}}$	$q_{\widetilde{-}}, a_\pm$	
class–$a_{\widetilde{+}}$	$\square_{a_{\widetilde{+}}}$	$q_{\widetilde{+}}, a_\pm$	
class–$\infty_{\widetilde{+}}$	$\square_{\infty_{\widetilde{+}}}$	$a_{\widetilde{+}}$	connecting to n-bundled ss-saddle
class–$\infty_{\widetilde{-}}$	$\square_{\infty_{\widetilde{-}}}$	$a_{\widetilde{-}}$	connecting to n-bundled ss-saddle

4. Local orbit structures for flows and COT symbols and algorithm. We show that a discrete graph, called *partially Cyclically Ordered Tree* (COT for short), is provided uniquely to every flow of finite type with an n-bundled ss-saddle based on the mathematical theory in section 3. To this end, we define symbolic notations, called *COT symbols,* to express orbit structures in $\mathrm{Bd}^h(v)$ and $(\mathrm{Bd}^h(v))^c$. which are grouped into several classes as listed in Table 4.1.

4.1. Two-dimensional orbit structures in $(\mathrm{Bd}^h(v))^c$. Based on Theorem 3.10, we distinguish a uniform flow box, a transverse annulus, and a periodic annulus. We regard a uniform box in Figure 3.5(a) as the default structure and no symbol is provided.

Figure 4.1(a) is a transverse source annulus, to which $b_{\widetilde{+}}(\square_{\widetilde{+}}, \{\square_{a_{\widetilde{+}}s}\})$ is assigned as its COT symbol. The subscript $\widetilde{+}$ of b indicates that it is a source annulus. The square symbol $\square_{\widetilde{+}}$ indicates that a source structure belonging to class–$\widetilde{+}$ in Table 4.1 is embedded as its internal orbit structure. In addition, by $\square_{a_{\widetilde{\pm}}s}$, we express that any number ($s \geq 0$) of class–$a_{\widetilde{\pm}}$ orbit structures can be embedded in the open annulus. To be more specific, $\square_{a_{\widetilde{\pm}}s}$ is expressed by

$$\square_{a_{\widetilde{\pm}}s} := \square^1_{a_{\widetilde{\pm}}} \cdot \cdots \cdot \square^s_{a_{\widetilde{\pm}}} \quad (s>0), \qquad \square_{a_{\widetilde{\pm}}s} := \lambda_\sim \quad (s=0), \tag{4.1}$$

in which the symbol $\square^i_{a_{\widetilde{\pm}}}$ denotes the ith class–$a_{\widetilde{\pm}}$ orbit structure. The symbol $\lambda_\sim$ is used to express the nonexistence of class-$a_{\widetilde{\pm}}$ orbit structures. The arrangement of class–$a_{\widetilde{\pm}}$ orbit structures is cyclic, which is expressed by enclosing (4.1) in the parentheses $\{\}$. Let us note that the square symbols in the COT symbol will be replaced with the COT symbols of the inner structures when they are identified in the algorithm presented in section 4.4. Figure 4.1(b) is a transverse sink annuls whose COT symbol is given by $b_{\widetilde{-}}(\square_{\widetilde{-}}, \{\square_{a_{\widetilde{-}}s}\})$, in which $\square_{\widetilde{-}}$ and $\square_{a_{\widetilde{-}}s}$ denote a class–$\widetilde{-}$ sink structure inside and class–$a_{\widetilde{-}}$ orbit structures of (4.1) in the annulus, respectively.

The COT symbol of a counterclockwise periodic annulus in Figure 4.1(c) is given by $b_+(\square_{\alpha_+})$, where $\square_{\alpha_+}$ denotes a class–α_+ orbit structure inside the inner boundary. For a

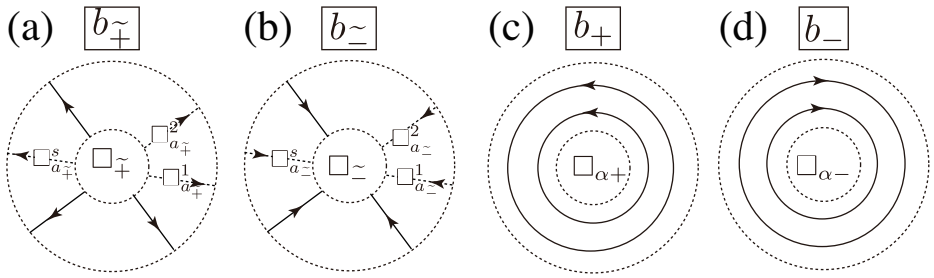

Figure 4.1. *Two-dimensional orbit structures in* $(\mathrm{Bd}^h(v))^c$. (a) *A transverse source annulus whose COT symbol is* $b_{\tilde{+}}(\square_{\tilde{+}}, \{\square_{a\tilde{+}s}\})$. (b) *A transverse sink annulus whose COT symbol is* $b_{\tilde{-}}(\square_{\tilde{-}}, \{\square_{a\tilde{-}s}\})$. (c, d) *An open periodic annulus whose COT symbol is* $b_{\pm}(\square_{\alpha\pm})$.

clockwise periodic annulus in Figure 4.1(d), the COT symbol is $b_-(\square_{\alpha-})$ with a class–α_- orbit structure inside.

4.2. Zero-dimensional and 1D orbit structures. We introduce COT symbols to orbit structures in the set of border orbits $\mathrm{Bd}^h(v)$.

4.2.1. Singular orbits ($\sigma_\pm, \sigma_{\tilde{\pm}\pm}, \sigma_{\tilde{\pm}0}, \infty_{\tilde{\pm}}$). Nondegenerate singular orbits are centers, sources, and sinks as shown in Figure 4.2(a). The COT symbol of a center having counterclockwise (resp., clockwise) periodic orbits in its neighborhood is given by σ_+ (resp., σ_-). When a source is associated with counterclockwise (resp., clockwise) orbits, its COT symbol is denoted by $\sigma_{\tilde{+}+}$ (resp., $\sigma_{\tilde{+}-}$). For a sink surrounded by a clockwise (resp., counterclockwise) orbit, we assign the COT symbol $\sigma_{\tilde{-}-}$ (resp., $\sigma_{\tilde{-}+}$). The COT symbol of a source (resp., a sink) associated with nonrotating orbits is $\sigma_{\tilde{+}0}$ (resp., $\sigma_{\tilde{-}0}$). On the other hand, we assign the same COT symbol $\infty_{\tilde{\pm}}$ to the n-bundled ss-saddle as shown in Figure 4.2(b), although its structure depends on n. This is because there exists only one n-bundled ss-saddle in the flow as a result of gluing boundary, which is uniquely identified as a COT symbol of the root structure as in section 4.3.

4.2.2. One-dimensional orbit structures ($p_{\tilde{\pm}}$, $p_\pm$, $a_{\tilde{\pm}}$). We provide COT symbols for 1D orbit structures that appear in the 2D blood flow patterns in section 5. The other structures are shown in Appendix A.

When a limit cycle is surrounded by periodic orbits outside, it is necessarily associated with a transverse annulus inside. Otherwise, it cannot be a limit cycle. The COT symbol of this orbit is given by $p_{\tilde{+}}(\square_{b\tilde{\pm}})$ (resp., $p_{\tilde{-}}(\square_{b\tilde{\pm}})$) when the flow direction of the limit cycle is counterclockwise (resp., clockwise), in which $\square_{b_{\tilde{\pm}}}$ denotes the transverse annulus of class–$b_{\tilde{\pm}}$ embedded as shown in Figure 4.3(a). On the other hand, when a limit cycle is surrounded by nonclosed orbits outside as in Figure 4.3(b), the internal orbit structure is either a periodic annulus or a transverse annulus. The COT symbol of the counterclockwise (resp., clockwise) limit cycle is then given by $p_+(\square_{b+})$ (resp., $p_-(\square_{b-})$), in which $\square_{b\pm}$ symbolizes a 2D orbit structure of class–$b_\pm$.

We consider a slidable saddle connecting to two source structures (resp., sink structures). When the saddle and the two source (resp., sink) structures are connected as in Figure 4.3(c), we provide $a_{\tilde{+}}\{\square_{\tilde{+}}, \square_{\tilde{+}}\}$ (resp., $a_{\tilde{-}}\{\square_{\tilde{-}}, \square_{\tilde{-}}\}$) as its COT symbol. Let us remark that the

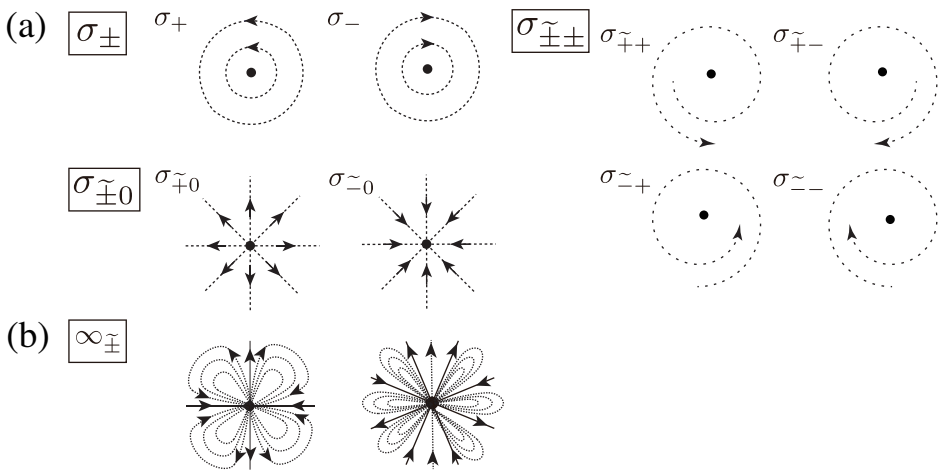

Figure 4.2. (a) *Nondegenerate zero-dimensional orbit structures. Centers surrounded by counterclockwise (resp., clockwise) periodic orbits are denoted by* σ_+ *(resp.,* σ_-*). A source and a sink having counterclockwise/clockwise/nonrotating nonclosed orbits in its neighborhood are represented by* $\sigma_{\tilde{\pm}+}/\sigma_{\tilde{\pm}-}/\sigma_{\tilde{\pm}0}$*.* (b) *Degenerate n-bundled ss-saddles. The same COT symbol* $\infty_{\tilde{\pm}}$ *is used for these degenerate points.*

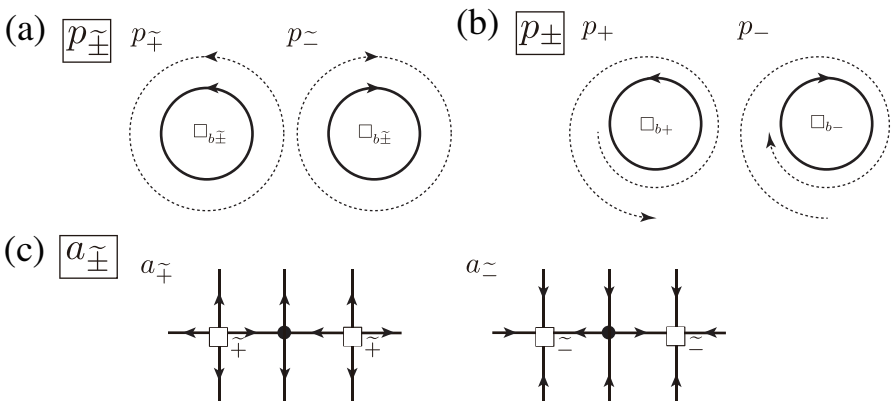

Figure 4.3. (a) *A limit cycle surrounded by periodic orbits outside and attracting/repelling orbits inside. Its COT symbol is given by* $p_{\tilde{+}}(\square_{b\tilde{\pm}})$ *(resp.,* $p_{\tilde{-}}(\square_{b\tilde{\pm}})$*) when the flow direction of the limit cycle is counterclockwise (resp., clockwise).* (b) *A limit cycle surrounded by attracting/repelling nonclosed orbits outside. The orbit structures inside are either of a periodic annulus or a transverse annulus. Its COT symbol is* $p_+(\square_{b+})$ *(resp.,* $p_-(\square_{b-})$*) for the limit cycle going in the counter-clockwise (resp., clockwise) direction.* (c) *Orbit structures with a slidable saddle. The saddle and two sources (sink) structures are connected by ss-separatrices, whose COT symbols are given by* $a_{\tilde{\pm}}\{\square_{\tilde{\pm}}, \square_{\tilde{\pm}}\}$*. They are in double-sign correspondence.*

n-bundled ss-saddle can be one of the source/sink structures connecting to the slidable saddle. Then the COT symbol is expressed by $a_{\tilde{\pm}}\{\square_{\tilde{\pm}}, \infty_{\tilde{\pm}}\}$. Note also that both source/sink structures cannot be the degenerate singular orbit simultaneously, since it is a special orbit structure appearing in the root structures.

4.3. Root structures on the spherical surface S.

Root structures are fundamental orbit structures appearing in the flow of finite type with an n-bundled ss-saddle.

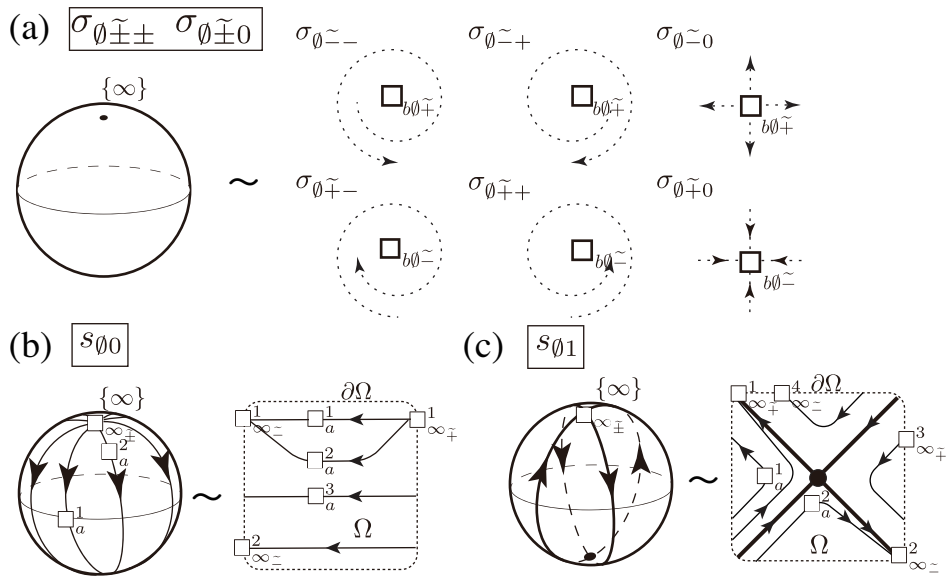

Figure 4.4. *Root structures.* (a) *A flow on the spherical surface S (or an open disk Ω) with a source (resp., a sink) orbit structure. Its COT symbol is either $\sigma_{\emptyset\tilde{\mp}0}(\square_{b\emptyset\tilde{\pm}})$, $\sigma_{\emptyset\tilde{\mp}-}(\square_{b\emptyset\tilde{\pm}})$, or $\sigma_{\emptyset\tilde{\mp}+}(\square_{b\emptyset\tilde{\pm}})$, in which $\square_{b\emptyset\tilde{\pm}} = b_{\tilde{\pm}}(\square_{\tilde{\pm}}, \{\square_{a\tilde{\pm}s}\})$ denotes the source/sink structures in Ω. Since the singular orbit at $\{\infty\}$ is a sink (resp., a source), the flow domain becomes a transverse annulus. Double signs correspond.* (b) *Root structure $s_{\emptyset 0}$, which is a flow with a 0-bundled ss-saddle at $\{\infty\}$. We can embed any number of triplets $\square_{a\infty\tilde{\pm}} := [\square_{\infty_{\tilde{\mp}}}, \square_{as}, \square_{\infty_{\tilde{-}}}]$ corresponding to uniform flow orbits consisting of class–a orbit structures between a source and a sink orbit structures. The COT symbol for the root structure in this panel is given by $s_{\emptyset 0}([\square^1_{\infty_{\tilde{\mp}}}, \square^1_a \cdot \square^2_a, \square^1_{\infty_{\tilde{-}}}], [\infty_{\tilde{\mp}}, \square^3_a, \infty_{\tilde{-}}], [\infty_{\tilde{\mp}}, \lambda_\sim, \square^2_{\infty_{\tilde{-}}}])$.* (c) *Root structure $s_{\emptyset 1}$, which is a flow with a 1-bundled ss-saddle. The four ss-saddle separatrices between the saddle and the 1-bundled ss-saddle separate the flow domain into four disjoint uniform flow boxes, in which we can embed any number of uniform flows with nontrivial orbit structures represented by the set of triplets. The COT symbol for this panel is given by $s_{\emptyset 1}\{[\square^1_{\infty_{\tilde{\mp}}}, \lambda_\sim, \infty_{\tilde{-}}] \cdot [\infty_{\tilde{\mp}}, \square^1_a, \infty_{\tilde{-}}], [\infty_{\tilde{\mp}}, \square^2_a, \square^2_{\infty_{\tilde{-}}}], [\square^3_{\infty_{\tilde{\mp}}}, \lambda_\sim, \infty_{\tilde{-}}], [\infty_{\tilde{\mp}}, \lambda_\sim, \square^4_{\infty_{\tilde{-}}}]\}$.*

4.3.1. Root structures $\sigma_{\emptyset\tilde{\pm}0}$ and $\sigma_{\emptyset\tilde{\pm}\pm}$.

When no n-bundled ss-saddle exists on the spherical surface S, there exists a pair of a source (resp., a sink) structure in S, as symbolized by $\square_{b\emptyset\tilde{+}}$ (resp., $\square_{b\emptyset\tilde{-}}$) as in Figure 4.4(a), and a sink (resp., a source) at $\{\infty\}$. The orbit structure is then topologically equivalent to a transverse annulus. Hence, the COT symbol of the inner structure is specified by $\square_{b\emptyset\tilde{\pm}} := b_{\tilde{\pm}}(\square_{\tilde{\pm}}, \{\square_{a\tilde{\pm}s}\})$. We distinguish the rotational direction around the singular orbit at $\{\infty\}$ in the COT symbols. When the orbit structure $\square_{b\emptyset+}$ (resp., $\square_{b\emptyset-}$) is a source (resp., a sink) structure associated with nonrotating nonclosed orbits, we provide $\sigma_{\emptyset\tilde{-}0}(b_{\tilde{+}}(\square_{\tilde{+}}, \{\square_{a\tilde{+}s}\}))$ (resp., $\sigma_{\emptyset\tilde{+}0}(b_{\tilde{-}}(\square_{\tilde{-}}, \{\square_{a\tilde{-}s}\}))$) to the root structure. On the other hand, when the orbit structure $\square_{b\emptyset+}$ (resp., $\square_{b\emptyset-}$) is a source (resp., a sink) structure consisting of nonclosed orbits rotating in the counterclockwise direction, the flow around $\{\infty\}$ becomes a sink (resp., a source) associated with clockwise orbits. Then, the symbol $\sigma_{\emptyset\tilde{-}-}(b_{\tilde{+}}(\square_{\tilde{+}}, \{\square_{a\tilde{+}s}\}))$ (resp., $\sigma_{\emptyset\tilde{+}-}(b_{\tilde{-}}(\square_{\tilde{-}}, \{\square_{a\tilde{-}s}\}))$) is assigned to the root structure. Reversing the flow direction, we obtain a source (resp., a sink) at $\{\infty\}$ associated with counterclockwise orbits with the COT symbol $\sigma_{\emptyset\tilde{+}+}(b_{\tilde{-}}(\square_{\tilde{-}}, \{\square_{a\tilde{-}s}\}))$ (resp., $\sigma_{\emptyset\tilde{-}+}(b_{\tilde{+}}(\square_{\tilde{+}}, \{\square_{a\tilde{+}s}\}))$).

4.3.2. Root structures $s_{\emptyset n}(n=0,1)$. When there exists an n-bundled ss-saddle at $\{\infty\}$, we obtain $4n$ saddle separatrices connecting n saddles in S and the degenerate singular orbit. We here explain the root structures for $n=0,1$, since they practically appear in 2D blood flow patterns obtained by echocardiography VFM. See Appendix A for a general description of the root structure for $n \geq 2$.

For $n=0$, all orbits in S connect a dipole singularity at $\{\infty\}$ as shown in Figure 4.4(b). The root structure is equivalent to a uniform flow box in an open disk Ω with a transversal boundary condition, in which we can embed 1D orbit structures between source/sink orbit structures of class–$\infty_{\tilde{\pm}}$ at the boundary $\partial\Omega$. Moreover, for each 1D orbit structure between the source/sink structures, any number ($s \geq 0$) of class–a orbit structures can exist. To express these 1D orbit structures, we introduce the following triplet notation:

$$\square_{a\infty\tilde{\pm}} := [\square_{\infty_{\tilde{\mp}}}, \square_{as}, \square_{\infty_{\tilde{-}}}], \tag{4.2}$$

which indicates that $s(\geq 0)$ local orbit structures $\square_{as}$ of class–a exist between a source structure $\square_{\infty_{\tilde{\mp}}}$ and a sink structure $\square_{\infty_{\tilde{-}}}$ at $\partial\Omega$. If no source or sink structure exists, we use $\infty_{\tilde{\pm}}$ for $\square_{\infty_{\tilde{\pm}}}$. For the symbol $\square_{as}$, we use

$$\square_{as} := \square_a^1 \cdot \square_a^2 \cdot \cdots \cdot \square_a^s \quad (s>0), \qquad \square_{as} := \lambda_{\sim} \quad (s=0), \tag{4.3}$$

where the COT symbol of the ith class–a orbit structure is expressed by $\square_a^i$. Moreover, since the root structure can contain any number ($s \geq 0$) of triplets in Ω, we provide the COT symbol $s_{\emptyset 0}(\square_{a\infty\tilde{\pm}s})$ to this structure, where $\square_{a\infty\tilde{\pm}s}$ denotes the arrangement of the triplets:

$$\square_{a\infty\tilde{\pm}s} := \square^1_{a\infty\tilde{\pm}} \cdot \cdots \cdot \square^s_{a\infty\tilde{\pm}} \quad (s>0), \qquad \square_{a\infty\tilde{\pm}s} = \lambda_{\sim} \quad (s=0).$$

As an example, the root structure of Figure 4.4(b) contains three 1D orbit structures, which are expressed by $[\square^1_{\infty_{\tilde{\mp}}}, \square^1_a \cdot \square^2_a, \square^1_{\infty_{\tilde{-}}}]$, $[\infty_{\tilde{\mp}}, \square^3_a, \infty_{\tilde{-}}]$ and $[\infty_{\tilde{\mp}}, \lambda_{\sim}, \square^2_{\infty_{\tilde{-}}}]$.

For $n=1$, the four ss-saddle separatrices are connected between the saddle in S and the 1-bundled ss-saddle at $\{\infty\}$ as shown in Figure 4.4(c). Remember that the four saddle separatrices divide the flow domain into four elliptic sectors, in which we can embed any number of 1D orbit structures connecting the 1-bundled ss-saddle. To express the orbit structures in these elliptic sectors, we also use the triplet notation (4.2). By arranging the orbit structures in the four disjoint domains in the counter-clockwise direction, we obtain the COT symbol for the root structure:

$$s_{\emptyset 1}\left\{\square^1_{a\infty\tilde{\pm}s}, \square^2_{a\infty\tilde{\pm}s}, \square^3_{a\infty\tilde{\pm}s}, \square^4_{a\infty\tilde{\pm}s}\right\}. \tag{4.4}$$

Note that, in each $\square^i_{a\infty\tilde{\pm}s}$, we arrange the triplets from the orbit structure nearest to the saddle. For instance, we have $\square^1_{a\infty\tilde{\pm}s} = [\square^1_{\infty_{\tilde{\mp}}}, \lambda_{\sim}, \infty_{\tilde{-}}] \cdot [\infty_{\tilde{\mp}}, \square^1_a, \infty_{\tilde{-}}]$, $\square^2_{a\infty\tilde{\pm}s} = [\infty_{\tilde{\mp}}, \square^2_a, \square^2_{\infty_{\tilde{-}}}]$, $\square^3_{a\infty\tilde{\pm}s} = [\square^3_{\infty_{\tilde{\mp}}}, \lambda_{\sim}, \infty_{\tilde{-}}]$ and $\square^4_{a\infty\tilde{\pm}s} = [\infty_{\tilde{\mp}}, \lambda_{\sim}, \square^4_{\infty_{\tilde{-}}}]$ for the root structure in Figure 4.4(c).

4.4. Conversion algorithm to COT representations. Suppose that we have border orbits of the flow of finite type v on a disk Ω satisfying the transversal boundary condition, and obtain the ss-saddle connection diagram $D_{ss}(v)$. Then we apply the following algorithm to $D_{ss}(v)$:

(Step 1) For all innermost sources/sinks and centers, we create nodes with labels $\sigma_{\tilde{\mp}\pm}$, $\sigma_{\tilde{\mp}0}$, and $\sigma_{\pm}$ depending on orbit structures around them. We then remove the orbit structures from the image of $D_{ss}(v)$ and replace them with a "blank"($\square$) symbol. After this step, all zero-dimensional orbit structures are replaced by blank symbols.

(Step 2) For each 1D and 2D orbit structure containing only blank symbols as their inner structures, we remove this orbit structure from the image of $D_{ss}(v)$ and replace it with a blank symbol. We then create a node corresponding to the orbit structure and introduce directed edges from this node as a parent to the child nodes of their inner orbit structures. The label of the parent node is obtained by substituting the labels of the child nodes into the corresponding square symbols in the COT symbol of the parent node. This step is repeated inductively until all orbit structures except the n-bundled ss-saddle are removed.

(Step 3) If there contain no saddles in Ω, the root structure is $\sigma_{\emptyset\tilde{\mp}\pm}$ in Figure 4.4(a), or $s_{\emptyset 0}$ in Figure 4.4(b). For the former case, we proceed to Step 4. For the latter case, we proceed to Step 5. Otherwise, the root structure is $s_{\emptyset n}$. We proceed to Step 6.

(Step 4) The root structure is a transverse annulus in Figure 4.4(a). If it is a transverse source annulus associated with counterclockwise/clockwise/nonrotating orbit structure, the root structure is $\sigma_{\emptyset\tilde{-}+}/\sigma_{\emptyset\tilde{-}-}/\sigma_{\emptyset\tilde{-}0}$. On the other hand, for a transverse sink annulus with counterclockwise/clockwise/nonrotating orbit structure, it is $\sigma_{\emptyset\tilde{+}+}/\sigma_{\emptyset\tilde{+}-}/\ \sigma_{\emptyset\tilde{+}0}$. We create the root node for this structure and direct edges to all child nodes of the inner structures. The label of the root node is obtained by substituting the labels of the child nodes into the square symbols in the COT symbol of the root structure. Then the label of the root node becomes the COT representation for the given flow of finite type. The algorithm terminates.

(Step 5) The root structure is a uniform flow box in Figure 4.4(b). We create the root node. Identifying the embedded uniform flow structures in Ω, we generate nodes from which we create direct edges to child notes corresponding to uniform flow structures. The label of the root node is obtained by substituting the triplet labels corresponding to the child nodes into the blank of $s_{\emptyset 0}$, which yields the COT representation. The algorithm terminates.

(Step 6) The root structure is a flow of the finite type with an n-bundled ss-saddle for $n=1$ in Figure 4.4(c) and $n \geq 2$ in Figure A.2. We create the root node. The $4n$ ss-saddle separatrices of the n saddles divide the flow domain Ω into $3n+1$ disjoint uniform flow boxes. For each uniform flow box, we express uniform flow structures in the domain as the triplets (4.2) and create directed edges from the root node to the triplet nodes. The COT representation is obtained as the label of the root node $s_{\emptyset n}$ by arranging the triplets as (4.4) and (A.2). The algorithm terminates.

Here we see how the algorithm works with an example. Figure 4.5(a) is a flow pattern of echocardiography VFM, where we extract border orbits in the ss-saddle connection diagram $D_{ss}(v)$. A schematic of $D_{ss}(v)$ after the topological preconditioning is shown in Figure 4.5(b), to which we apply the algorithm. In Step 1, we find a clockwise sink (a red point) on the left-hand side of $D_{ss}(v)$. Hence, we create a node with the label $\sigma_{\tilde{-}-}$ for the orbit structure and replace it with a blank ($\square$) symbol as in Figure 4.5(c). In Step 2, we find a slidable saddle connecting the blank sink symbol and a boundary sink point $\infty_{\tilde{-}}$, which is shown as red

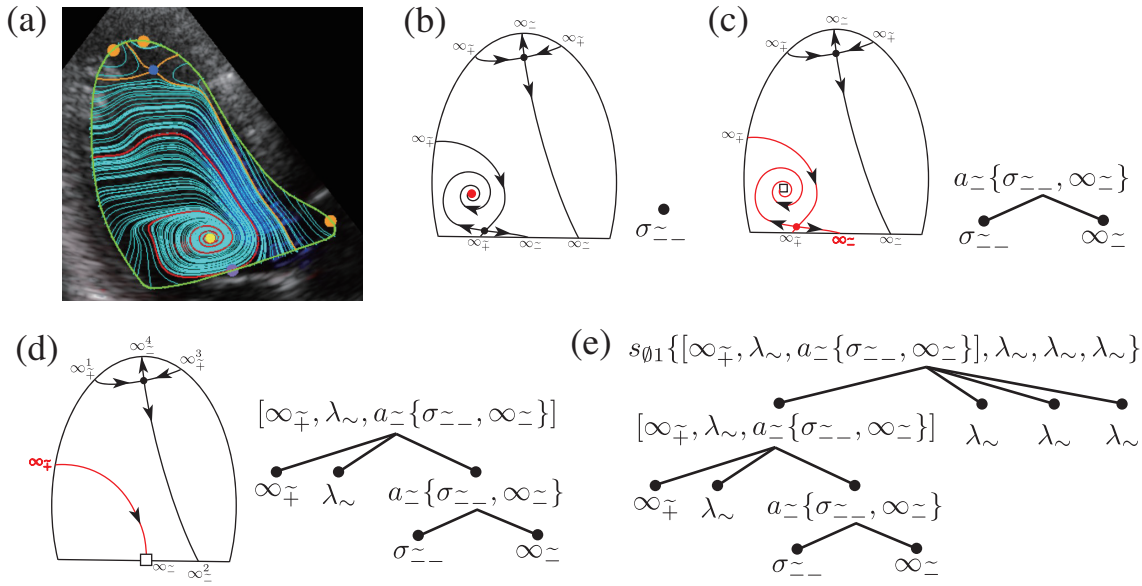

Figure 4.5. (a) *A flow pattern obtained by echocardiography VFM with border orbits in* $D_{ss}(v)$. (b) *(Left) A schematic of* $D_{ss}(v)$ *extracted from the flow pattern after the topological preconditioning. (Right) In Step* 1*, we find a clockwise sink (a red point) and create a node for it. Since no other sinks/sources/centers exist, we proceed to Step* 2. (c) *(Left) In Step* 2*, we find a slidable saddle structure* $a_{\sim}$ *(red curves with a saddle) and (right) create its corresponding node and two edges to the nodes of the inner structures. Since no one-dimensional* (1*D*) *orbit structures exist, we proceed to Step* 3. (d) *(Left) In Step* 3*, we identify the root structure as* $s_{\emptyset 1}$ *and proceed to Step* 6*. We find a uniform flow structure (a red curve). (Right) This structure is expressed by a triplet.* (e) *Embedding the triplet, we obtain a tree named COT for this flow pattern, where the label of the root node becomes the COT representation.*

curves with a saddle in Figure 4.5(c). Creating a node corresponding to this orbit structure, we introduce edges to the child nodes with the labels $\sigma_{\sim\,-}$ and $\infty_{\sim}$. Also, setting $\square^1_{\sim} = \sigma_{\sim\,-}$ and $\square^2_{\sim} = \infty_{\sim}$ in the COT symol $a_{\sim}\{\square^1_{\sim}, \square^2_{\sim}\}$ as the inner structures, we obtain the label of this node as $a_{\sim}\{\sigma_{\sim\,-}, \infty_{\sim}\}$. We replace the slidable saddle connecting to the boundary with the blank symbol $\square_{\infty_{\sim}}$ at the boundary, which gives rise to a uniform flow orbit (a red curve) represented by the triplet $[\infty_{\mp}, \lambda_{\sim}, a_{\sim}\{\sigma_{\sim\,-}, \infty_{\sim}\}]$ as in Figure 4.5(d). In Step 3, since only one saddle is associated with four ss-separatrices crossing the boundary transversely, the root structure is identified as $s_{\emptyset 1}$. Hence, proceeding to Step 6, we finally create the root node linking the triplet node. Consequently, arranging the triplet as (4.4) in cyclic order, we obtain a tree, i.e., COT in Figure 4.5(e). The label of the root node becomes the COT representation:

$$s_{\emptyset 1}\left\{[\infty_{\mp}, \lambda_{\sim}, a_{\sim}\{\sigma_{\sim\,-}, \infty_{\sim}\}], \lambda_{\sim}, \lambda_{\sim}, \lambda_{\sim}\right\}. \tag{4.5}$$

It is important to remark that every topological orbit structure generated by the flow of finite type with an n-bundled ss-saddle is a one-to-one correspondence with a COT representation. This fact is mathematically proven as discussed in Appendix B. Hence, the COT representation is a unique identifier of the topological structures. In addition, since the COT expresses the configuration of border orbits separating the flow domain as a tree structure as

in Figure 4.5(e), we can extract geometric features of flow domains based on it as we see in section 5.

5. Application to blood flow patterns measured by the echocardiography VFM. As discussed in sections 2.1 and 2.2, it is known that typical vortex flow patterns appear in the LV in systole and diastole. During systole, a large vortex in the basal portion is formed to facilitate smooth outflow, and its disturbance is known to be the result of deterioration of the LV function, and during diastole, trans-mitral inflow forms a "vortex ring" inside LV, resulting in a twin vortex beneath the anterior and posterior mitral leaflet, which is changed with flow efficiency after the heart valve surgery. Here, based on the COT representations, we figure out the configuration of the vortex structure as a result of the blood flow ejection and filling in the LV.

5.1. Decomposition of domains in 2D blood flow in the LV. Figure 5.1(a) is an original flow pattern obtained by echocardiography VFM. As we see in section 4.4, the COT representation is given by

$$s_{\emptyset 1}\left\{[\infty_{\tilde{+}}, \lambda_{\sim}, a_{\tilde{-}}\{\sigma_{\tilde{-}-}, \infty_{\tilde{-}}\}], \lambda_{\sim}, \lambda_{\sim}, \lambda_{\sim}\right\}. \tag{5.1}$$

We note that the COT representation is more than a unique symbolic/graphical identifier of the topological flow structure. It yields clinically useful image processing for 2D blood flow patterns. Figure 5.1(b) shows the decomposition of the flow domain obtained based on the COT representation, where each domain corresponds to the 2D flow components separated by the border orbits associated with the COT symbols. A large flow domain painted red on the left-hand side represents a vortical flow region separated by ss-separatrices of the slidable saddle $a_{\tilde{\pm}}$ in the triplet of (5.1). We refer to the vortical flow region as a *topological vortex structure*. In medical science, as discussed in section 2.3, it is important to identify such a vortical flow domain generated by the heartbeat, since it can be used to measure cardiac function as a pump of blood flow. Hence, the identification of topological vortex structures is a useful image processing brought by the TFDA with the COT representations.

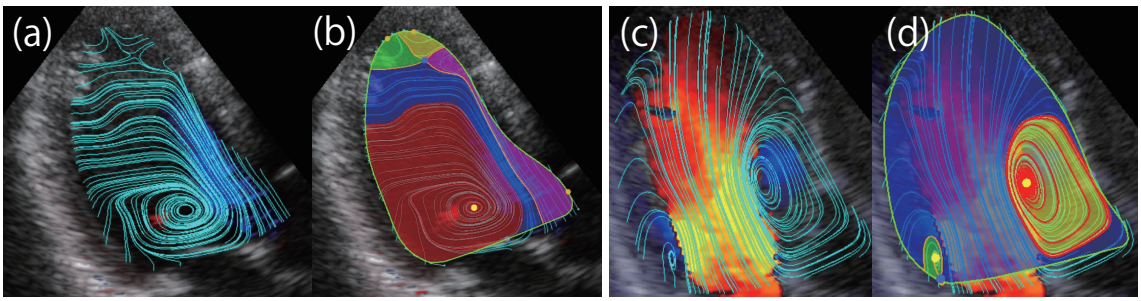

Figure 5.1. (a) *A flow pattern in systole obtained by echocardiography VFM.* (b) *Decomposition of the flow domain based on the COT representation. The large red region expresses a topological vortex structure associated with the* $a_{\tilde{+}}$ *symbol in the triplet of* (5.1). (c) *A flow pattern in diastole obtained by echocardiography VFM.* (d) *Decomposition of the flow domain based on the COT representation. The blue and the purple regions are the topological vortex structures associated with the* $a_{\tilde{+}}$ *symbols in the triplets of* (5.2).

Another example is a flow pattern in diastole in Figure 5.1(c), in which we observe a strong upward flow associated with two clockwise/counterclockwise vortical source structures at both sides of the region. Applying the conversion algorithm to the flow pattern of Figure 5.1(c), we obtain the COT representation for this flow pattern:

$$s_{\emptyset 0}([a_{\tilde{+}}\{\sigma_{\tilde{+}+}, \infty_{\tilde{+}}\}, \lambda_{\sim}, \infty_{\tilde{-}}], [\infty_{\tilde{+}}, \lambda_{\sim}, a_{\tilde{-}}\{\sigma_{\tilde{-}-}, \infty_{\tilde{-}}\}]), \tag{5.2}$$

which gives rise to the decomposition of the flow domain in Figure 5.1(d). We thus identify two topological vortex structures represented by $a_{\tilde{+}}\{\sigma_{\tilde{+}+}, \infty_{\tilde{+}}\}$ and $a_{\tilde{-}}\{\sigma_{\tilde{-}-}, \infty_{\tilde{-}}\}$ in the triplets, which correspond to the flow domains painted green and yellow in Figure 5.1(d), respectively. They correspond to a section of a large vortex ring structure generated by the inflow of blood.

5.2. Description of healthy and disease cases. The COT representations describe the differences in intracardiac vortex flow patterns between healthy and heart failure cases in terms of topological vortex structures. As an example, we consider one of the typical diseases that cause heart failure: dilated cardiomyopathy cases. Since the essential pathophysiology of heart failure is the insufficiency of ejected blood from the LV, we focus on the flow pattern in systole. In Figure 5.2, the upper row illustrates flow patterns with the ss-saddle connection diagram, in which nondegenerate source/sinks as yellow points and saddles as blue points, while the lower row shows the decomposition of the flow domain based on the COT representations.

Figure 5.2(a) is the flow pattern of a healthy heart in systole, which is the same as Figure 5.1(a, b). The large topological vortex structures represented by $a_{\tilde{-}}\{\sigma_{\tilde{-}-}, \infty_{\tilde{-}}\}$ in the

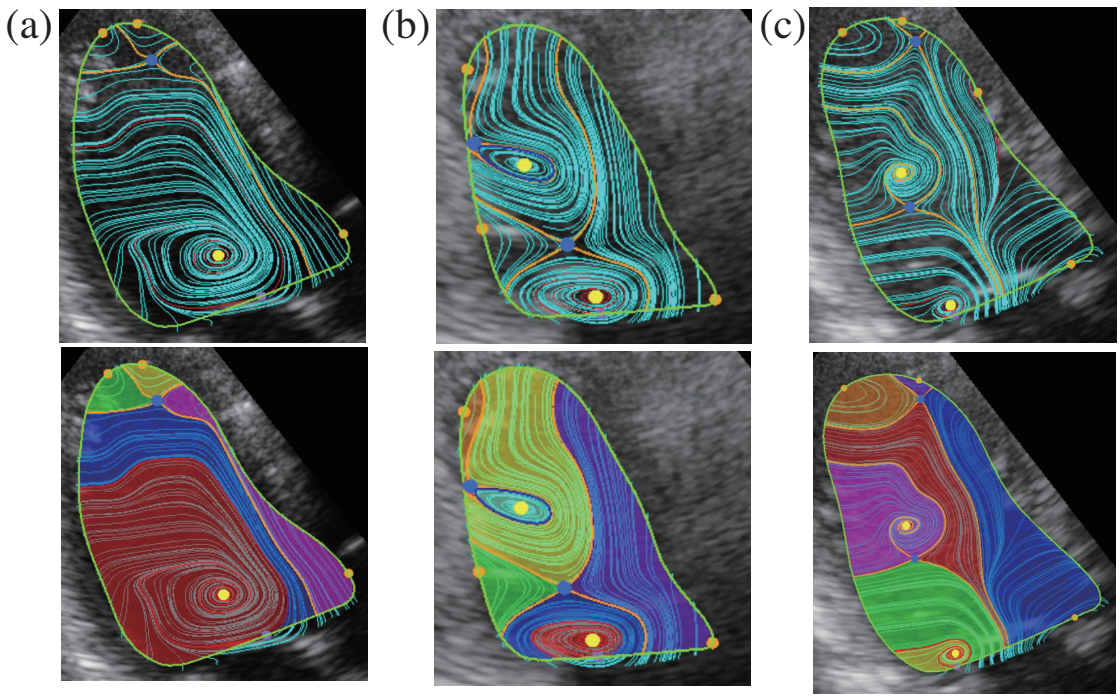

Figure 5.2. *Systolic vortex flow patterns with the ss-saddle connection diagram and decompositions of flow domains based on the COT representation.* (a) *A healthy heart;* (b, c) *heart failure cases.*

triplet of (5.1) is identified as the red domain in a posterior basal portion. It facilitates a smooth outflow toward the aortic valve, which is supposed to be efficient.

Next, a heart failure case in Figure 5.2(b) has a different flow pattern. Its COT representation is given by

$$s_{\emptyset 1}\left\{[\infty_{\tilde{+}}, \lambda_{\sim}, a_{\tilde{-}}\{\sigma_{\tilde{-}-}, \infty_{\tilde{-}}\}], \lambda_{\sim}, [a_{\tilde{+}}\{p_{-}(b_{\tilde{+}}(\sigma_{\tilde{+}-}, \lambda_{\sim})), \infty_{\tilde{-}}\}], \lambda_{\sim}\right\}. \tag{5.3}$$

There exists a small topological vortex structure (a red domain) represented by $a_{\tilde{-}}\{\sigma_{\tilde{-}-}, \infty_{\tilde{-}}\}$ in the basal posterior wall. It is the same topological vortex structure as observed in the healthy LV, but the vortex becomes immature in its size because the LV function is insufficient. This means that the topological vortex structure is not supposed to generate an efficient ejection flow drive. In addition, we observe another vortex structure containing a limit cycle as an inner structure (an orange domain and a blue domain) in the apical portion, which is represented by $a_{\tilde{+}}\{p_{-}(b_{\tilde{+}}(\sigma_{\tilde{+}-}, \lambda_{\sim})), \infty_{\tilde{-}}\}$. It is also supposed to disturb smooth ejection through the aortic valve. The saddle of the root structure $s_{\emptyset 1}$ moves toward the basal posterior wall, indicating an inefficient flow different from the healthy flow pattern. Here, it is important to remark that the COT representation can express a complex configuration of the topological vortex structure. In this example, the COT representation (5.3) indicates that the apical topological vortex structure in Figure 5.2(b) is not a simple basin of attraction, but it contains the limit cycle as an inner structure.

Another heart failure case in Figure 5.2(c) contains two topological vortex structures, whose COT representation is given by

$$s_{\emptyset 1}\left\{[\infty_{\tilde{+}}, \lambda_{\sim}, a_{\tilde{-}}\{\sigma_{\tilde{-}-}, \infty_{\tilde{-}}\}] \cdot [\infty_{\tilde{+}}, \lambda_{\sim}, a_{\tilde{-}}\{\sigma_{\tilde{-}-}, \infty_{\tilde{-}}\}], \lambda_{\sim}, \lambda_{\sim}, \lambda_{\sim}\right\}. \tag{5.4}$$

It shows that two topological vortex structures exist on the left-hand side of the LV. This means the topological vortex structure observed in the healthy heart in systole splits, forming a large topological vortex structure (a cyan domain) in the mid portion of the LV apart from the small one (a yellow domain) in the aortic valve. As a result, this flow pattern again disturbs efficient blood ejection toward the aortic valve. The location of the saddle and its ss-saddle separatrix defining the root structure $s_{\emptyset 1}$ is similar to that in the healthy LV, but the immature vortex formation in the basal portion causes separated small two regions of topological vortex structures, resulting in disturbed flow ejection.

Although differences in geometrical configurations are visually apparent from flow patterns, the COT representations elucidate the domains of vortical flow structures in blood flows and express their complex inner orbit structure as a tree and COT symbols, thereby evaluating clinically useful vortex structures and their associated quantities such as the area and locations of these regions measuring the efficiency of blood flows. In this sense, it has advantages in qualitative and quantitative studies of ventricular functions in cardiac diseases.

6. Summary. We have developed a new mathematical theory classifying topological orbit structures of two-dimensional flows in a disk with a moving boundary. The theory is generally utilized for various complex flows with a pulsate pump and ejection/injection that appear in engineering problems. In this paper, we use the theory of the blood flow in the LV of the heart measured by echocardiography and 4D MRI, which is an important medical application. Since

the flow is generated by contraction and relaxation of the heart muscle with inflow/outflow through the mitral and aortic valves, the orbits of the flow appear to cross the boundary transversely by measurements. This means that the preceding topological classification theory for the flows of finite type on spherical surfaces [22], in which the orbits are assumed to be tangent along the boundary, is no longer applicable. We have resolved this problem by introducing a degenerate singular orbit, named an n-bundled ss-saddle. We then introduce the flow of finite type with an n-bundled ss-saddle on the spherical surface S without solid boundaries, or equivalently the flow of finite type on an open disk Ω with a transversal boundary condition as a mathematical model of blood flows in a 2D section of the LV obtained by echocardiography VFM or 4D flow MRI. This is a new topological classification theory suitable for blood flows in the LV.

Based on the topological classification theory, we succeed to construct an algorithm converting any given flow of finite type with an n-bundled ss-saddle into a unique symbolic expression, named COT representation. The COT representations give rise to symbolic expressions of topological orbit structures, and they also realize an image processing capturing topological vortex structures corresponding to $a_{\mp}$ symbols in the triplets. These vortex structures coincide well with the flow structures observed conventionally by clinical experts. Since the topological vortex structures persist robustly, the regions captured by TFDA are kept unchanged under any small disturbances. Furthermore, one can make a quantitative comparison among topological vortex structures in terms of areas, shapes, and locations of structures. Comparison with TFDA to blood flow data of heart failures enables us to explain physiology and pathophysiology in terms of COT representations and their corresponding topological vortex structures. We are now developing software that realizes the image processing presented here, and its application to practical clinical data related to heart diseases will be reported in the near future.

Appendix A. Other orbit structures in the flow of finite type with an n-bundled ss-saddle.

A.1. Orbit structure with a homoclinic saddle ($a_{\pm}$, $b_{\pm\pm}$, $b_{\pm\mp}$). Figure A.1(a) shows an orbit structure consisting of a self-connected counterclockwise (resp., clockwise) saddle separatrix and two ss-separatrices connecting to a source and a sink structures. Its COT symbol becomes $a_+(\square_{b+})$ (resp., $a_-(\square_{b-})$), in which $\square_{b+}$ (resp., $\square_{b-}$) indicates that a class–b_+ (resp., class–b_-) structure is embedded inside the self-connected saddle separatrix.

When a saddle is connected by two self-connected saddle separatrices, it forms a figure eight pattern as in Figure A.1(b). Depending on the direction of the self-connected saddle separatrices, we assign the COT symbol $b_{++}\{\square_{b+},\square_{b+}\}$ or $b_{--}\{\square_{b-},\square_{b-}\}$, in which $\square_{b\pm}$ represents the embedded class–$b_{\pm}$ orbit structures inside the saddle separatrices. They are enclosed by the parentheses $\{\}$ owing to their cyclic arrangement. When one self-connected saddle separatrix encloses another self-connected saddle separatrix as in Figure A.1(c), the COT symbol $b_{+-}(\square_{b+},\square_{b-})$ is assigned to this structure when the outer saddle separatrix is going in the counterclockwise direction. Reversing the flow direction, we obtain an orbit structure with a saddle, represented by $b_{-+}(\square_{b-},\square_{b+})$.

A.2. Orbit structures with a saddle ($q_{\pm}$, $q_{\mp}$). When a counterclockwise (resp., clockwise) self-connected saddle separatrix encloses two ss-saddle separatrices connecting to a

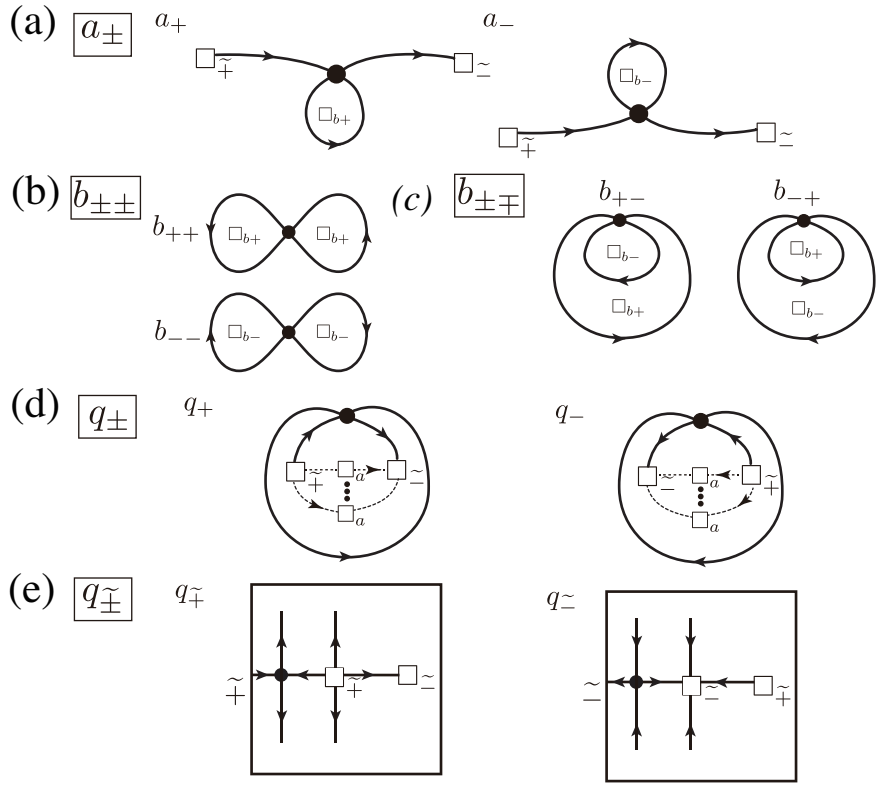

Figure A.1. (a) *Orbit structures with a self-connected saddle separatrix. The saddle has two ss-separatrices connecting to a source and a sink structure outside the self-connected saddle separatrix, whose COT symbol is given by* $a_\pm(\square_{b\pm})$. (b) *Figure eight orbit structures with two self-connected saddle separatrices, whose COT symbols are given by* $b_{\pm\pm}\{\square_{b\pm},\square_{b\pm}\}$. (c) *Orbit structures in which one self-connected saddle separatrix is enclosed by the other self-connected saddle separatrix. The COT symbols are given by* $b_{\pm\mp}(\square_{b\pm},\square_{b\mp})$. (d) *Orbit structures with a self-connected saddle separatrix. The saddle has two saddle separatrices connecting to a source and a sink structures inside the self-connected saddle separatrix, whose COT symbol is* $q_\pm(\square_{\tilde{\mp}},\square_{\tilde{=}},\square_{as})$. *The subscript* $\pm$ *of* a *and* q *corresponds to the direction of the self-connected saddle separatrix.* (e) *Orbit structures with a slidable saddle. A saddle and one source/sink structure are contained inside the other source/sink structure, whose COT symbol is given by* $q_{\tilde{\pm}}(\square_{\tilde{\pm}})$. *The structure* $q_{\tilde{\pm}}$ *can be embedded only in a transverse source/sink annulus* $b_{\tilde{\pm}}$. *They are in double-sign correspondence.*

source and a sink structures as shown in Figure A.1(d), we provide $q_+(\square_{\tilde{\mp}},\square_{\tilde{=}},\square_{as})$ (resp., $q_-(\square_{\tilde{\mp}},\square_{\tilde{=}},\square_{as})$) as the COT symbol of this structure, in which $\square_{\tilde{\pm}}$ and $\square_{as}$ denote the source/sink structures and the arrangement of class–a orbit structures (4.3), respectively.

We finally consider another slidable saddle connecting two source structures or two sink structures. See Figure A.1. If the saddle and one source (resp., sink) structure are contained in the other source (resp., sink) structure as in Figure A.1(e), its COT symbol is given by $q_{\tilde{\mp}}(\square_{\tilde{\mp}})$ (resp., $q_{\tilde{=}}(\square_{\tilde{=}})$). The orbit structures can be embedded only in a transverse annulus.

A.3. Root structure $s_{\emptyset n}(n \geq 2)$. For $n \geq 2$, the $4n$ ss-saddle separatrices between the n-saddles and the n-bundled ss-saddle divide the whole surface into $3n+1$ disjoint domains, in which triplet orbit structures of $\square_{a\infty\tilde{\pm}s}$ are embedded. While the arrangement of sectors

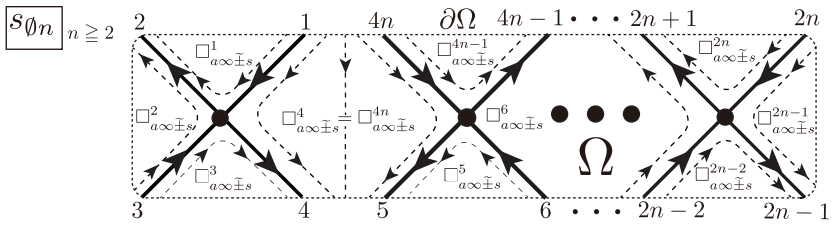

Figure A.2. *Other root structure $s_{\emptyset n}$, which is a flow with an n-bundled ss-saddle ($n \geq 2$). The $4n$ ss-saddle separatrices divide the whole domain into $3n+1$ disjoint open flow boxes. Arranging the orbit structures in the counter-clockwise order, we obtain the COT symbol (A.2) for the root structure.*

in $s_{\emptyset 0}$ and $s_{\emptyset 1}$ is uniquely defined, the arrangement of sectors in the root structure of $s_{\emptyset n}$ ($n \geq 2$) depends on how we construct the n-bundled ss-saddle as explained in Figure 3.2(d). We thus explain how to arrange the sectors in the COT representation using Figure A.2, in which n saddles are arranged in a row as an example. We first choose an ss-saddle separatrix that is transverse to the boundary $\partial\Omega$. Starting from the ss-saddle separatrix, we enumerate $4n$ ss-saddle separatrices in the counterclockwise direction along the boundary. Since these transverse points at the boundary are collapsed to the degenerate n-bundled ss-saddle by gluing the boundary, all ss-saddles are connected to the degenerate point.

By construction, there exist $2n+2$ domains whose boundary comprises two ss-saddle separatrices between the n-bundled ss-saddle and one saddle. An example is the flow domain enclosed by the first and the second ss-saddle separatrices in Figure 4.4(d). The orbit structure in the domain becomes an elliptic sector with respect to the n-bundled ss-saddle, in which one can embed the triplet orbit structures represented by (4.2). On the other hand, the remaining $n-1$ domains are enclosed by four ss-saddle separatrices connecting the n-bundled ss-saddle and two different saddles, as we see the flow domain bounded by the saddle separatrices 4, 5, $4n$, and 1 in Figure 4.4(d). In these subdomains, all orbit structures go across the flow domain in one direction, which gives rise to parabolic sectors with respect to the n-bundled ss-saddle. To express the orbit structures in parabolic sectors, we use a different triplet notation,

$$\square_{a\infty\tilde{\pm}} := \langle \square_{\infty_{\tilde{\mp}}}, \square_{as}, \square_{\infty_{\tilde{-}}} \rangle. \tag{A.1}$$

The COT representation of this root orbit structure is provided as follows. Suppose that the flow domain enclosed by the kth and $(k+1)$th ss-saddle separatrices of the same saddle is an elliptic sector. Then, the triplet notation (4.2) is used to express orbit structures embedded in the elliptic sector. On the other hand, if the kth and $(k+1)$th ss-saddle separatrices are connecting to different saddles, the flow domain becomes a parabolic sector and we thus embed the triplet orbit structures of (A.1). Repeating this process fr $k=1$ to $4n$ and arranging the triplet notations in order, we obtain

$$s_{\emptyset n}\left\{\square^1_{a\infty\tilde{\pm}s}, \square^2_{a\infty\tilde{\pm}s}, \square^3_{a\infty\tilde{\pm}s}, \ldots, \square^{4n-1}_{a\infty\tilde{\pm}s}, \square^{4n}_{a\infty\tilde{\pm}s}\right\}. \tag{A.2}$$

The rule of arranging orbit structures in the COT representation is determined uniquely up to cyclic order. We note that the triplet orbit structures in $n-1$ parabolic sectors appear twice in the COT representation. For instance, the orbit structure in the parabolic sectors

for the fourth ss-saddle separatrix is equivalent to that for the $4n$th ss-saddle separatrix, i.e., $\square^4_{a\infty\tilde{\pm}s} = \square^{4n}_{a\infty\tilde{\pm}s}$. This is redundant, but arranging the triplet orbit structures in a cyclic order without ambiguity is beneficial. Hence, when we reconstruct the topological orbit structures from the COT representation, we need to avoid picking up the redundant structures.

Appendix B. One-to-one correspondence with COT representations. It is shown that topological orbit structures generated by the flows of finite type (without any degenerate singular orbit) are in many-to-one correspondence with COT representations in [22]. To make it one-to-one, we need additional information named *the linking strcture.* The linking structure, whose definition is presented in [22] and not shown here, is another graph representation expressing how ss-components in $D_{ss}(v)$ are connected. We can compute the linking structure in the same way regardless of the existence of an n-bundled ss-saddle. Hence, we have the following result.

Theorem B.1. *The topological orbit patterns of the flow of finite type with an n-bundled ss-saddle on a spherical surface without boundaries are in one-to-one correspondence with pairs of a COT representation and a linking structure.*

From the viewpoint of practical data analysis, it is sufficient to compute the COT representation and to draw a schematic picture of the ss-saddle connection diagram $D_{ss}(v)$ instead of computing the linking structure, since the linking structure is substantially expressed by this schematic picture as discussed in [22].

Acknowledgments. The second author is a founder and technical advisor of Cardio Flow Design Inc. The author would like to thank Dr. Teruyasu Nishino, Dr. Shohei Miyazaki, and Dr. Ben Dyer in Cardio Flow Design Inc. for their support in the implementation of the TFDA algorithm in VFM according to the industry-academia collaboration. The author would also like to thank Dr. Koichi Akiyama, Dr. Hideyuki Hayashi, and Dr. Hiroo Takayama for providing healthy and heart failure case data of echocardiography.

REFERENCES

[1] K. Akiyama, N. Nakamura, K. Itatani, Y. Naito, M. Kinoshita, M. S. S. Hamaoka, H. Kato, H. Yasumoto, Y. Nakajima, T. Mizobe, S. Numata, H. Yaku, and T. Sawa, *Flow-dynamics assessment of mitral-valve surgery by intraoperative vector flow mapping*, Int. Cardiovasc. Thorac. Surg., 6 (2017), pp. 869–875.
[2] H. Aref and M. Brøns, *On stagnation points and streamline topology in vortex flows*, J. Fluid Mech., 370 (1998), pp. 1–27.
[3] A. V. Bolsinov and A. T. Fomenko, *Integrable Hamiltonian Systems: Geometry, Topology, Classification*, CRC Press, Boca Raton, FL, 2005.
[4] J. S. Cho, S. Shrestha, N. Kagiyama, L. Hu, Y. A. Ghaffar, G. Casaclang-Verzosa, I. Zeb, and P. P. Sengupta, *A network-based "phenomics" approach for discovering patient subtypes from high-throughput cardiac imaging data*, JACC Cardiovasc. Imaging, 8 (2020), pp. 1955–1670.
[5] G. Gutierrez, *Smoothing continuous flows on two-manifolds and recurrences*, Ergodic Theory Dyn. Syst., 6 (1986), pp. 17–44.
[6] K. Itatani, *When the blood flow becomes bright*, Euro. Heart J., 35 (2014), pp. 747–752a.
[7] K. Itatani, *Advances in Hemodynamic Research*, Nova Science Publisher, Hauppauge, NY, 2015.
[8] K. Itatani, T. Okada, T. Uejima, T. Tanaka, M. Ono, K. Miyaji, and K. Takenaka, *Intraventricular flow velocity vector visualization based on the continuity equation and measurements of vorticity and wall shear stress*, Jpn. J. Appl. Phys., 52 (2013), 07HF16.

[9] R. Kakizaki, T. Nabeta, S. Ishii, T. Koitabashi, K. Itatani, T. Inomata, and J. Ako, *Cardiac resynchronization therapy reduces left ventricular energy loss*, Int. J. Cardiol., 221 (2016), pp. 546–548.
[10] A. Kheradvar, M. Milano, and M. Gharib, *Correlation between vortex ring formation and mitral annulus dynamics during ventricular rapid filling*, ASAIO J., 53 (2007), pp. 8–16.
[11] R. Kidambi and P. K. Newton, *Streamline topologies for integrable vortex motion on a sphere*, Phys. D, 140 (2000), pp. 95–125.
[12] T. Ma and S. Wang, *A generalized poincaré–hopf index formula and its applications to* 2*-d incompressible flows*, Nonlinear Anal. Real World Appl., 2 (2001), pp. 467–482.
[13] T. Ma and S. Wang, *Geometric Theory of Incompressible Flows with Applications to Fluid Dynamics*, Math. Surveys Monogr. 119, AMS, Providence, RI, 2005.
[14] A. Maier, *Trajectories on the closed orientable surfaces*, Rec Math. [Mat. Sbornik] N.S. (Russian, with English summary), 12 (1943), pp. 71–84.
[15] K. Moffatt, *The topology of scalar fields in* 2*d and* 3*d turbulence*, in *Proceedings of IUTAM Symposium Geometry and Statistics of Turbulence (Hayama)*, Fluid Mech. Appl. 59, T. K., et al., eds., Kluwer Academic Publishers, Dordrecht, 2001, pp. 13–22.
[16] T. Nabeta, K. Itatani, K. Miyaji, and J. Ako, *Vortex flow energy loss reflects therapeutic effect in dilated cardiomyopathy*, Eur. Heart J., 36 (2015), p. 637.
[17] K. Nakaji, K. Itatani, N. Tamaki, H. Morichi, N. Nakanishi, M. Takigami, M. Yamagishi, H. Yaku, and K. Yamada, *Assessment of biventricular hemodynamics and energy dynamics using lumen-tracking* 4*d flow mri without contrast medium*, J. Cardiol., 78 (2021), pp. 79–87.
[18] I. Nikolaev, *Foliations on Surfaces*, A Series of Modern Surgeys in Mathematics 41, Springer-Verlag, Berlin, Heidelberg, 2001.
[19] T. Sakajo, S. Ohishi, and T. Uda, *Identification of kuroshio meanderings south of japan via a topological data analysis for sea surface height*, J. Oceanography, (2022).
[20] T. Sakajo, Y. Sawamura, and T. Yokoyama, *Unique encoding for streamline topologies of incompressible and inviscid flows in multiply connected domains*, Fluid Dyn. Res., 46 (2014), p. 031411.
[21] T. Sakajo and T. Yokoyama, *Tree representation of topological streamline patterns of structurally stable* 2*d hamiltonian vector fields in multiply connected domains*, IMA J. Appl. Math., 83 (2018), pp. 380–411.
[22] T. Sakajo and Y. Yokoyama, *Discrete representations of orbit structures of flows for topological data analysis discrete representations of orbit structures of flows for topological data analysis*, Discrete Math. Algorithms Appl., 15 (2023), 2250143, https://doi.org/10.1142/S1793830922501439.
[23] T. Uda, T. Sakajo, M. Inastu, and K. Koga, *Morphological identification of atmospheric blockings via topological flow data analysis*, J. Meteo. Soc. Japan, 99 (2021), pp. 1169–1183.
[24] T. Yokoyama, *Decompositions of Surface Flows*, preprint, https://arxiv.org/abs/1703.05501, 2020.
[25] T. Yokoyama and T. Sakajo, *Word representation of streamline topologies for structurally stable vortex flows in multiply connected domains*, Proc. R. Soc. Lond. Ser. A Math. Phys. Eng. Sci, 469 (2013), 20120558.